UNIVERSITY OF LEEDS

This is a repository copy of *Bio-geographic climate sensitivity controls Earth system response to Large Igneous Province carbon degassing*.

White Rose Research Online URL for this paper:
https://eprints.whiterose.ac.uk/215106/

Version: Accepted Version

Article:

Rogger, J., Judd, E.J., Mills, B.J.W. orcid.org/0000-0002-9141-0931 et al. (3 more authors) (2024) Bio-geographic climate sensitivity controls Earth system response to Large Igneous Province carbon degassing. Science, 385 (6709). pp. 661-666. ISSN 0036-8075

https://doi.org/10.1126/science.adn3450

This is the author’s version of the work. It is posted here by permission of the AAAS for personal use, not for redistribution. The definitive version was published in Science on Vol 385, Issue 6709, 8 Aug 2024, DOI: 10.1126/science.adn3450.

Reuse
Items deposited in White Rose Research Online are protected by copyright, with all rights reserved unless indicated otherwise. They may be downloaded and/or printed for private study, or other acts as permitted by national copyright laws. The publisher or other rights holders may allow further reproduction and re-use of the full text version. This is indicated by the licence information on the White Rose Research Online record for the item.

Takedown
If you consider content in White Rose Research Online to be in breach of UK law, please notify us by emailing eprints@whiterose.ac.uk including the URL of the record and the reason for the withdrawal request.

White Rose
university consortium
Universities of Leeds, Sheffield & York

eprints@whiterose.ac.uk
https://eprints.whiterose.ac.uk/

Title: Bio-geographic climate sensitivity controls Earth system response to Large Igneous Province carbon degassing

Authors: Julian Rogger[1,2*], Emily J. Judd[3], Benjamin J.W. Mills[4], Yves Goddéris[5], Taras V. Gerya[1], Loïc Pellissier[2,6]

Affiliations:

[1]Department of Earth Sciences, ETH Zurich, Zurich, Switzerland.

[2]Department of Environmental Systems Science, ETH Zurich, Zurich, Switzerland.

[3]Smithsonian National Museum of Natural History, Department of Paleobiology, Washington, DC, USA.

[4]University of Leeds, School of Earth and Environment, Leeds, United Kingdom.

[5]Géosciences-Environnenment Toulouse, CNRS-Observatoire Midi-Pyrénées, Toulouse, France.

[6]Swiss Federal Institute for Forest, Snow and Landscape Research, Birmensdorf, Switzerland.

*Corresponding author. Email: julian.rogger@erdw.ethz.ch

Abstract: Periods of Large Igneous Province (LIP) magmatism have shaped Earth's biological and climatic history, causing major climatic shifts and biological reorganizations. The vegetation response to LIP-induced perturbations may affect the efficiency of the carbon-climate regulation system and the post-LIP climate evolution. Using an eco-evolutionary vegetation model, we demonstrate that the vegetation's climate adaptation capacity, through biological evolution and geographic dispersal, is a major determinant of the severity and longevity of LIP-induced hyperthermals, and can promote the emergence of a new climatic steady state. Proxy-based temperature reconstructions of the Permian-Triassic, Triassic-Jurassic and Paleocene-Eocene hyperthermals match the modelled trajectories of bio-climatic disturbance and recovery. We conclude that biological vegetation dynamics shape the multi-million-year Earth system response to sudden carbon degassing and global warming episodes.

Large Igneous Provinces (LIPs) represent major perturbations to the Earth system, triggering environmental changes that can result in severe mass extinctions on land and in the ocean (1, 2). Climate warming following the degassing of massive amounts of carbon in geologically instantaneous time is considered one of the main triggers of LIP-associated biological extinctions and reorganizations (1). The severity and duration of the climate perturbation depend on how fast the emitted carbon is returned to Earth's interior by climate feedback mechanisms such as silicate mineral weathering and organic carbon burial (3, 4). The efficiency of the carbon-climate regulation system, however, may in turn be affected by terrestrial and marine ecosystems being shifted to a state of disequilibrium and maladaptation (5–8).

The terrestrial vegetation plays an integral part in the long-term carbon-climate regulation system, but its functioning is sensitive to abrupt environmental changes. Primary productivity determines the extent of photosynthetic carbon assimilation and the burial of organic carbon as a net CO_2 sink. Vegetation can further enhance CO_2 consumption through silicate mineral weathering reactions, for example by releasing reactive species like organic acids and chelators into the soil during nutrient acquisition, or by intensifying the local hydrological cycle and prolonging water–mineral contact times (9–14). LIP-triggered environmental perturbations modify vegetation structure and functioning, causing species extinctions, range shifts, deforestation, reductions in organic carbon burial, and the spread of opportunistic species into newly freed habitats until more adapted plant communities reestablish (5–7, 15–17). To what extent and how fast vegetation functions recover from LIP-induced climatic changes depends on the capacity of plants to disperse and follow suitable habitats in a given paleogeographic setting (18) and to adjust to new conditions through evolutionary adaptation (19, 20). After the most severe mass extinction in Earth's history around 252 Ma ago, triggered by the Siberian Traps LIP, the recovery of vegetation diversity and productivity to pre-LIP levels required several million years (7, 15, 16). During this recovery period, the efficiency of the carbon-climate regulation system may have been reduced due to weakened vegetation–weathering interactions and reduced primary productivity. The long-term climatic consequences of LIP degassing events may be dictated not only by intrinsic characteristics of the LIP episode, such as the mass of emitted greenhouse gases, but also by the biological response and bio-climatic interactions in a given paleogeographic setting.

Here, we use an eco-evolutionary vegetation model and proxy-based temperature reconstructions to investigate how the climate adaptation capacity of vegetation, by dispersal and adaptive evolution, may have affected geologic carbon fluxes and the long-term climate evolution after episodes of Phanerozoic LIP degassing. We consider three LIPs, the Siberian Traps (Permian–Triassic boundary; ≈ 252 Ma), the Central Atlantic Magmatic Province (Triassic–Jurassic boundary; ≈ 201 Ma) and the North Atlantic Igneous Province (Paleocene–Eocene boundary; ≈ 56 Ma). The LIPs differed in the severity of the triggered biological and climatic consequences and occurred under contrasting paleogeographic configurations. During the Siberian Traps and the Central Atlantic Magmatic Province, most continental land mass was assembled in the supercontinent Pangea. The two LIPs are assumed to have caused two of the most severe mass extinctions in Earth's history (1). The Siberian Traps further resulted in a multi-million-year hyperthermal of elevated atmospheric CO_2 and temperatures (21, 22). The North Atlantic Igneous Province occurred under a more modern paleogeography with dispersed continents, and it caused the most severe warming event during the Cenozoic (Paleocene-Eocene Thermal Maximum, PETM) (23). While less severe in terms of species extinctions, it still induced a major reorganization of biological systems on land and in the ocean (24).

The eco-evolutionary model is designed to capture major vegetation dynamics in response to climate perturbations, including dispersal, adaptation and competition. It is coupled to models of the geologic carbon cycle and climate. The climate trajectory after an imposed LIP degassing episode depends on how fast the released carbon is returned from the atmosphere-ocean system to geologic carbon reservoirs through silicate weathering and organic carbon burial. Silicate weathering is modelled as a function of local erosion, runoff, temperature and vegetation-mediated weathering enhancement. In areas of high plant productivity, a maximum four-fold or six-fold (Supplementary Materials; SM) weathering enhancement is considered compared with unvegetated land (9, 10, 12, 25). Marine organic carbon production and burial depend on local sea surface temperatures and continental weathering as a nutrient source, while vegetation productivity and terrestrially derived organic carbon burial depend on solar radiation, aridity, temperature and the vegetation adaptation state. Primary productivity and weathering enhancement are calculated by modelling vegetation units that populate the continents and that can disperse and adapt in response to climatic changes at specified rates. The vegetation units represent plant assemblages, which we term 'floras', and depict the ensemble response of their constituents. Floras are characterized by a gaussian niche, defined by an optimum mean annual temperature (MAT) and Budyko aridity index (BAI) at which their physiological potential is greatest. The climate niche determines a geographic space in which a flora can be productive (niche range of 10°C in MAT and 2 BAI units; see SM and fig. S1 for derivation). The LIP-triggered climate warming can cause a discrepancy between a flora's optimum niche and the local environment, resulting in reduced productivity and vegetation-mediated weathering enhancement, until a better adapted flora disperses to the location, or the original flora adapts to the new conditions through adaptive evolution. By testing a wide parameter range for rates of flora dispersal (varying the scale parameter of the dispersal kernel between 0–100,000 km Ma^{-1}) and niche evolution (speed of temperature niche adaptation 0–10°C Ma^{-1}; aridity niche adaptation 0–100 BAI units Ma^{-1}), we explore the sensitivity of LIP-triggered climatic perturbations to the vegetation’s adaptation capacity in a given paleogeographic configuration.

Vegetation recovery shapes long-term climate trajectory and steady state

The vegetation's climate adaptation capacity and its effects on organic carbon burial and silicate weathering rates affect the severity and duration of the temperature excursion, as well as the long-term climatic steady state, after a LIP degassing event (fig. 1A). Using the paleogeography of the Permian-Triassic mass extinction and a LIP degassing of 40,000 Gt of carbon in 200 ka (3), modelled global average surface temperature (GAST) warming is between 7°C and 12°C, with greater warming in simulations in which floras have a limited capacity to disperse in geographic space or to adapt their climatic niche to local environmental conditions by adaptive evolution. The climate trajectories recovered from the simulations show four categories of behavior (fig. 1B): the 'return', 'die out', 'new quasi-steady state', and 'transient' trajectories. 'Return' trajectories describe a full recovery of the GAST to temperatures similar to those before the degassing event. This scenario is characterized by an ephemeral temperature excursion during which carbon sinks temporarily fail to effectively remove carbon from the atmosphere-ocean system. This is caused by a vegetation adaptation lag, resulting in reductions in vegetation-mediated weathering enhancement and organic carbon burial. During the temperature excursion, these processes can temporarily offset the effects of higher temperatures and a more active hydrological cycle on silicate weathering. As the vegetation recovers, the strength of carbon feedback mechanisms is re-established, and excess carbon is effectively removed from the atmosphere-ocean system (complete set of carbon fluxes shown in fig. S2).

In a large proportion of the simulations, a 'new quasi-steady state' climate emerges, characterized by stabilization of the GAST at a higher temperature than before the degassing event. This scenario is characterized by carbon flux dynamics similar to those in the 'return' scenario, with the exception that the vegetation does not fully recover from the climatic perturbation. As a result, land-derived organic carbon burial and vegetation-mediated silicate weathering enhancement stabilize at a lower level than before the degassing event, resulting in a higher GAST. The new quasi-steady-state temperature is high enough that the direct climatic effects of temperature and increased runoff on silicate weathering counterbalance the solid Earth carbon degassing, despite the less adapted vegetation. A full vegetation recovery is prevented by the presence of dispersal barriers (e.g., oceans, deserts and areas with better-adapted competitors) that hinder floras in following their optimum climatic niche under a limited speed of *in situ* evolutionary adaptation. The resulting climate state is considered a quasi-steady state, as continued adaptive evolution, changes in degassing rates, or paleogeography beyond the considered model duration would promote further climatic changes.

The 'transient' category includes climate trajectories that reached neither the initial nor a new quasi-steady-state GAST within the modelled period but would presumably do so if a longer time horizon was considered. Finally, ’die out’ trajectories correspond to situations in which the terrestrial vegetation is not able to cope with the climatic changes and possibly vanishes completely. In this trajectory, temperatures continue to increase until silicate weathering can compensate for the carbon degassing in the absence of vegetation.

The trajectory of a LIP-triggered carbon-climate excursion is determined by the combination of the vegetation’s dispersal and climate adaptation capacity (fig. 1D). ‘Die out’ trajectories are limited to models assuming very low dispersal capacities. For temperature adaptation speeds lower than 1°C Ma^{-1}, simulations predict an increased likelihood of reaching a new climatic quasi-steady state. This is because the warming exceeds the *in situ* temperature adaptation capacity, thus triggering a dispersal response and a redistribution of floras, which can result in an incomplete recovery and less productive vegetation distribution. The aridity adaptation capacity limits the geographic space into which a flora can disperse. Therefore, simulations predict an increased proportion of transient trajectories with a slow climatic recovery in the low aridity adaptation range. We observe a full recovery from the climate perturbation only in simulations considering the highest dispersal and temperature adaptation rates, enabling floras to efficiently track their climatic niche or eliminate the need for migration, respectively. Such dispersal and temperature niche adaptation rates represent the upper end of what can be considered a plausible range for plants (18–20, 26, 27). Considering more likely temperature niche adaptation rates of 0–3° C Ma^{-1} (median below 1° C) (19, 26), non-zero aridity adaptation (19), and the exclusion of unrealistic dispersal values that result in ‘die out’ trajectories, all three of the categories ‘return’, ‘new quasi-steady state’ and ‘transient’ are plausible climate trajectories following a LIP degassing of the intensity estimated to have occurred at the Permian–Triassic boundary.

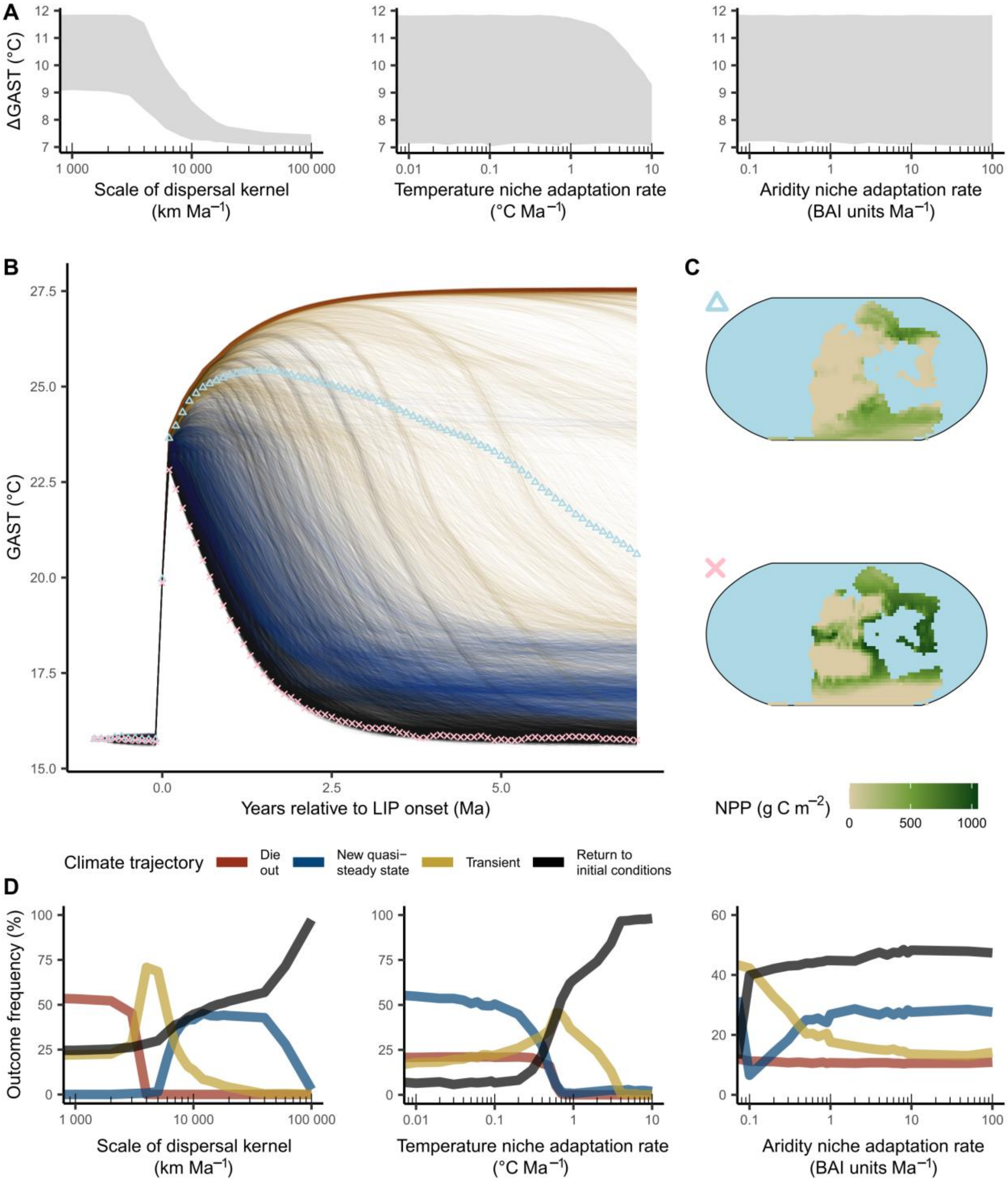

Figure 1: Sensitivity of modelled post-Large Igneous Province (LIP) climate trajectories to eco-evolutionary vegetation dynamics. A. Range of modelled global average surface temperature (GAST) increase depending on the terrestrial vegetation's adaptation capacity. The dispersal value represents the scale parameter of a Weibull distribution with shape parameter value of two, from which dispersal values of modelled floras are randomly drawn. A flora's aridity niche is characterized by a range of the Budyko aridity index (BAI). Aridity adaptation speed is thus expressed as BAI units per Ma. **B.** Range of climate trajectories observed for different vegetation adaptation capacities. Each line represents a separate model run with a different combination of vegetation dispersal and climatic niche adaptation capacity. 'Die out': model outcomes with less than 10^{12} mol C yr^{-1} terrestrial organic carbon burial at the end of the simulation and a high temperature steady state, 'return': complete recovery of climate from perturbation (ΔGAST between end and beginning of simulation < 0.5°C), 'new quasi-steady state': stabilization at a higher global average

temperature (minimum of +0.5°C compared to initial conditions, $\Delta GAST < 0.5°C$ and $\Delta F_{locb} < 5 \cdot 10^{10}$ mol C yr^{-1} during the last two million model years), 'transient': none of the above occurs until the end of the simulation. All carbon fluxes associated with the different climate trajectories are shown in fig. S2. **C.** Spatial net primary productivity (NPP) plots showing the distribution of productivity for a 'return' (bottom) and a 'transient' (top) scenario 2 Ma after the LIP onset. **D.** Model outcome frequency depending on biological adaptation parameters. In total, 12,122 parameter combinations were tested (19 Weibull dispersal scale parameters, and 29 temperature- and 22 aridity-adaptation rates).

Bio-climatic response to Phanerozoic LIPs

Simulations produce climate trajectories that correspond well with the variable temperature responses reconstructed for different Phanerozoic LIPs (fig. 2). We compiled multi-million-year composite sea surface temperature reconstructions spanning the emplacement and aftermath of the Siberian Traps, the Central Atlantic Igneous Province and the North Atlantic Igneous Province LIPs based on several geochemical proxy systems and from different locations around the globe (see SM). We applied the coupled vegetation–carbon-cycle model to the corresponding paleogeographic settings and varied boundary conditions, i.e., pre-LIP atmospheric CO_2 concentration and mass and duration of the LIP carbon degassing, within estimated ranges [600 ppm, 40,000 Gt C, 200 ka, for the Siberian Traps (21, 28, 29), 800 ppm, 30,000 Gt C, 200 ka, for the Central Atlantic Igneous Province (30, 31) and 500 ppm, 15,000 Gt C, 100 ka (step injection) (32–34), for the North Atlantic Igneous Province, respectively; alternative scenarios in fig. S3]. In doing so we identify eco-evolutionary vegetation dynamics as a possible cause of the variability in post-LIP climate evolution – excluding models with unrealistic dispersal scales that would result in 'die-out' trajectories and considering only models with non-zero temperature and aridity niche adaptation rates.

Geologic proxies suggest the most severe and sustained warming for the Siberian Traps (Permian-Triassic), with temperatures increasing by 5–10°C over 5 Ma following the LIP and a subsequent recovery of temperatures to about 2.5°C higher than before the LIP. This severity and multi-million-year warming, as well as a possible shift to a new climate quasi-steady state, is reproduced in the model when a strongly impacted vegetation with a limited climate adaptation capacity by dispersal and evolution is assumed, resulting in a sustained reduction of the efficiency of the carbon-climate regulation system. The resulting reduction in the ratio of organic to total carbon burial further results in an excursion of approximated carbonate $\delta^{13}C$ signatures, in agreement with proxy records for the period (up to −6 ‰; fig. S4). Applying the same biological parameter space to the Central Atlantic Igneous Province (Triassic-Jurassic), we simulate less severe temperature excursions, with an initial warming of around 5°C and a relatively rapid and continuous recovery of temperatures thereafter, in line with the proxy data. This suggests a faster recovery of vegetation and carbon-cycle feedback mechanisms after the LIP perturbation, with the excess carbon being captured effectively through silicate weathering and organic carbon burial. For the North Atlantic Igneous Province, the proxy record reveals a short-lived initial warming of

3–5°C (the PETM), followed by a multi-million-year increase in temperatures of approximately 2.5°C (the Early Eocene Climatic Optimum). This is in agreement with a large range of possible new climatic quasi-steady states modelled for the respective paleogeography. We further model a hypothetical LIP of 10,000 Gt C to test the response for the present-day continental configuration, assuming a starting CO_2 concentration of 400 ppm. Despite the lower mass of carbon injected, a similar set of trajectories as for the Permian-Triassic is observed, ranging from rapid recovery to very severe and sustained warming in models with a reduced biological adaptation capacity. This tendency for severe warming is caused by a particularly strong reduction in the carbon burial capacity following the LIP-triggered vegetation disturbance (fig. S5), and by the low initial CO_2 concentration that results in a sensitive temperature to CO_2 response (fig. S6), amplifying the warming and vegetation disturbance.

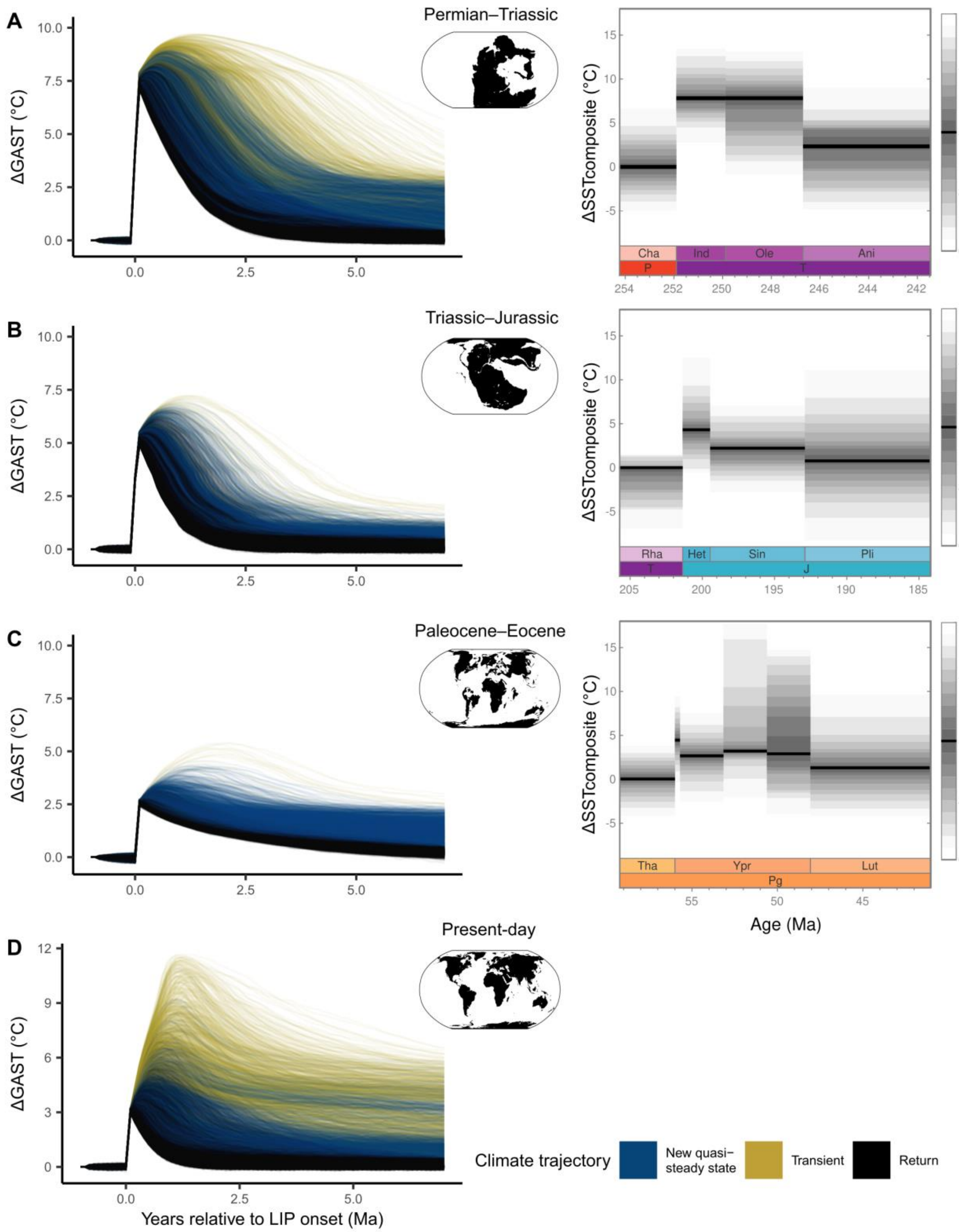

Figure 2: Comparison of modelled and reconstructed temperature changes for different Phanerozoic Large Igneous Province (LIP) degassing events. ΔGAST represents the change in the modelled global average surface temperature. $\Delta SST_{composite}$ represents a composite temperature change reconstructed from several geologic proxy systems and sample locations around the globe, based on data compiled in the PhanSST database (53); see Supplementary Materials for the derivation of temperature values. **A.** Siberian Traps LIP (Permian–Triassic boundary), **B.** the Central Atlantic Magmatic Province (Triassic–Jurassic boundary) and **C.** the North Atlantic Igneous Province (Paleocene–Eocene boundary). **D.** Hypothetical LIP scenario for present-day geography. See the main text for pre-LIP starting CO_2 concentration, LIP C degassing mass and LIP duration. An alternative set of scenarios

regarding the magnitude and duration of degassing, as well as sensitivity to plant weathering enhancement, is explored in fig. S3. Paleogeographies are taken from (54) and (55).

Bio-geographic climate sensitivity

Eco-evolutionary dynamics and climate evolution reveal strong interactions with the paleogeographic setting and LIP characteristics. Each geography is characterized by a distinct set of possible climate trajectories following a carbon injection (figs 2 & S3). Differences include the tendency for severe and persistent hyperthermals (e.g., Permian-Triassic and present-day configuration) or the chance to result in a warmer climatic quasi-steady state (e.g., Paleocene-Eocene). Our results suggest that these differences are caused by interacting biotic and abiotic factors. Abiotic and geographic factors include the magnitude of the LIP degassing event, the pre-event climate state (i.e., radiative forcing), and the response of temperature and the hydrological cycle to an increase in greenhouse gases (fig. S6). Together, these factors determine the severity of the initial climatic and biological perturbation. The recovery from this perturbation, however, is shaped by interacting biological and abiotic processes, as different geographic configurations cause different local environmental changes and stresses to the vegetation, but also shape recovery dynamics by determining possible migration routes. More fragmented continental configurations, like during the Paleocene-Eocene compared to supercontinent configurations, enhance the likelihood of a shift to a new climatic quasi-steady state, as dispersal barriers slow down biological recovery. Differences in the abundance and disturbance of regions with high rates of weathering and primary productivity tend to determine the efficiency of the post-LIP carbon regulation system and the resulting climatic evolution (figs S5 & S7). The coupled biotic and abiotic response to a perturbation can be considered a ‘bio-geographic’ climate sensitivity that is unique to every paleogeographic configuration and biota present in a given period.

Vegetation eco-evolution and the long-term carbon-climate system

By combining simulations and proxy-based climate reconstructions, we show how the evolution of the physical environment following a LIP-triggered perturbation is shaped by biological vegetation dynamics. Eco-evolutionary processes, including dispersal, evolution and competition, that determine the resilience and distribution of primary productivity and vegetation–weathering interactions can interfere with the carbon-climate regulation system, resulting in a large range of possible climate trajectories following a carbon cycle perturbation. The feedback documented here represents an important addition to the regulation mechanisms previously considered to shape the multi-million-year climate evolution following a massive carbon injection to Earth's atmosphere and oceans (3, 35–39).

LIP characteristics, paleogeography and eco-evolutionary vegetation dynamics combine to shape the temperature trajectories observed in simulations and the data for selected Phanerozoic LIPs. For the Permian–Triassic transition, we observe that the combination of the severe initial warming caused by the Siberian Traps and a limited vegetation adaptation capacity reduces the efficiency of the carbon regulation system and results in elevated atmospheric CO_2 and temperatures for several millions of years after the perturbation. Our temperature reconstruction and simulated scenarios are in agreement with other climatic reconstructions for the period (21, 22) and with the especially slow vegetation recovery observed in the fossil record in comparison to other extinction events (7, 15, 40, 41). After the Permian-Triassic mass extinction, it may have taken 4–5 Ma for stable forest ecosystems to re-establish (15, 42, 43). This could have played a particularly large role in slowing down the climatic recovery, considering the importance of deep-rooting trees in mediating plant–weathering interactions and carbon assimilation (13). In contrast, the geologic record and simulations indicate a faster recovery of temperatures for the Triassic-Jurassic hyperthermal, suggesting that the bio-geographic conditions permitted a faster equilibration and recovery of vegetation and the carbon-climate system. Other abiotic and biotic factors could have amplified differences in the vegetation response and climate evolution between the considered LIPs. Short-term 'kill mechanisms' such as acid rain, aerosol-induced climatic change, halogen toxicity, and increased levels of ultraviolet-B radiation could have reduced initial vegetation fitness and the ability of vegetation to respond to long-term climate changes (1, 44, 45). More severe climate warming is further modelled when floras are less adapted at the onset of the LIP, for example due to a previous climatic perturbation (fig. S9). Distinct environmental perturbations during the LIP emplacement result in different post-LIP plant community structures, with differences in functioning and ecological stability beyond the generalized vegetation response captured in the present model (40, 42, 43). Additional vegetation adaptation lags could be caused by a limited dispersal success, which is affected not only by the distribution of climatic zones, but also by the distribution and formation of appropriate soil conditions (42, 46) and the effect of climatic changes on dispersal vectors (47). Our results emphasize the importance of considering such LIP-triggered biological dynamics in shaping the Earth system response to severe warming.

The LIP-triggered vegetation response can cause a transition to a new climatic quasi-steady state. Combined simulations and data indicate that a new equilibrium can be reached after a multi-million-year high-temperature period (i.e., Permian-Triassic) or relatively rapidly after the initial carbon cycle perturbation, as observed for the Paleocene–Eocene transition. In contrast to the Siberian Traps, the floral recovery after the North Atlantic Igneous Province and the PETM is assumed to have occurred rapidly through plant dispersal (48) and less severely impacted plant communities (49). Our results indicate that, for variable speeds of the biological and climatic recovery, a main effect of LIPs is to trigger a process of vegetation turnover and reorganization that can change long-term rates of organic and inorganic carbon burial. These changes in carbon fluxes result in a new carbon cycle balance at a different atmospheric CO_2 level than before the perturbation (50, 51). Our findings are supported by limited climatic niche adaptation rates in plants, which are considerably lower than the warming rates during these events (19, 20). Hence, severe climate changes inevitably result in range shifts, competition and possibly the extinction of specific floras, which permanently alter the distribution and intensity of vegetation-mediated carbon fluxes. The vegetation reorganization may affect additional vegetation-climate interactions, which can contribute to a shift in the climate state. These include changes in surface albedo, affecting climate through an altered radiation balance [fig. S8; (52)], or changes in evapotranspiration rates and water cycling, which may further amplify the influence of vegetation shifts on weathering rates (fig. S3). Biological movement and vegetation dynamics are further shaped by the paleogeographic configuration, which affects the speed of biotic recovery and therefore the potential for long-term climatic shifts.

Throughout its history, Earth has experienced several severe mass extinctions and finds itself today in another major bio-climatic crisis – this time not triggered by a LIP, but by anthropogenic greenhouse gas emissions and land use. Our results show how the coupled response of biological systems and the abiotic environment shape the long-term consequences of such perturbations and reveal the possibility of a shift to a new climatic steady state.

References and Notes

1. D. P. Bond, P. B. Wignall, Large igneous provinces and mass extinctions: An update. *Volcanism, Impacts, and Mass Extinctions: Causes and Effects (Keller, G. and Kerr, A.C., eds.). Geological Society of America Special Paper 505*, DOI 10.1130/2014.2505(02) (2014).

2. M. J. Benton, Hyperthermal-driven mass extinctions: killing models during the Permian–Triassic mass extinction. *Philosophical Transactions of the Royal Society A: Mathematical, Physical and Engineering Sciences* **376**, 20170076, DOI 10.1098/rsta.2017.0076 (2018).

3. L. R. Kump, Prolonged Late Permian–Early Triassic hyperthermal: failure of climate regulation? *Philosophical Transactions of the Royal Society A: Mathematical, Physical and Engineering Sciences* **376**, 20170078, DOI 10.1098/rsta.2017.0078 (2018).

4. M. T. Jones, D. A. Jerram, H. H. Svensen, C. Grove, The effects of large igneous provinces on the global carbon and sulphur cycles. *Palaeogeography, Palaeoclimatology, Palaeoecology* **441**, 4–21, DOI 10.1016/j.palaeo.2015.06.042 (2016).

5. J. L. Payne *et al.*, Large Perturbations of the Carbon Cycle During Recovery from the End-Permian Extinction. *Science* **305**, 506–509, DOI 10.1126/science.1097023 (2004).

6. Z.-Q. Chen, M. J. Benton, The timing and pattern of biotic recovery following the end-Permian mass extinction. *Nature Geoscience* **5**, 375–383, DOI 10.1038/ngeo1475 (2012).

7. Z. Xu *et al.*, End Permian to Middle Triassic plant species richness and abundance patterns in South China: Coevolution of plants and the environment through the Permian–Triassic transition. *Earth-Science Reviews* **232**, 104136, DOI 10.1016/j.earscirev.2022.104136 (2022).

8. P. Hull, Life in the Aftermath of Mass Extinctions. *Current Biology* **25**, R941–R952, DOI 10. 1016/j.cub.2015.08.053 (2015).

9. L. L. Taylor *et al.*, Biological weathering and the long-term carbon cycle: integrating mycorrhizal evolution and function into the current paradigm. *Geobiology* **7**, 171–191, DOI 10.1111/j.1472-4669.2009.00194.x (2009).

10. K. L. Moulton, Solute flux and mineral mass balance approaches to the quantification of plant effects on silicate weathering. *American Journal of Science* **300**, 539–570, DOI 10.2475/ajs. 300.7.539 (2000).

11. J. Quirk, M. Y. Andrews, J. R. Leake, S. A. Banwart, D. J. Beerling, Ectomycorrhizal fungi and past high CO_2 atmospheres enhance mineral weathering through increased below-ground carbon-energy fluxes. *Biology Letters* **10**, 20140375, DOI 10.1098/rsbl.2014.0375 (2014).

12. E. Berner, R. Berner, K. Moulton, Plants and Mineral Weathering: Present and Past. *Treatise on Geochemistry* **5**, 169–188, DOI 10.1016/B0-08-043751-6/05175-6 (2003).

13. J. Quirk *et al.*, Constraining the role of early land plants in Palaeozoic weathering and global cooling. *Proceedings of the Royal Society B: Biological Sciences* **282**, 20151115, DOI 10.1098/rspb.2015.1115 (2015).

14. T. M. Lenton, M. Crouch, M. Johnson, N. Pires, L. Dolan, First plants cooled the Ordovician. *Nature Geoscience* **5**, 86–89, DOI 10.1038/ngeo1390 (2012).

15. L. Grauvogel-Stamm, S. R. Ash, Recovery of the Triassic land flora from the end-Permian life crisis. *Comptes Rendus Palevol* **4**, 593–608, DOI 10.1016/j.crpv.2005.07.002 (2005).

16. G. J. Retallack, J. J. Veevers, R. Morante, Global coal gap between Permian–Triassic extinction and Middle Triassic recovery of peat-forming plants. *Geological Society of America Bulletin* **108**, 195–207, DOI 10.1130/0016-7606(1996)108<0195:GCGBPT>2.3.CO;2 (1999).

17. P. McAllister Rees, Land-plant diversity and the end-Permian mass extinction. *Geology* **30**, 827, DOI 10.1130/0091-7613(2002)030<0827:LPDATE>2.0.CO;2 (2002).

18. R. T. Corlett, D. A. Westcott, Will plant movements keep up with climate change? *Trends in Ecology & Evolution* **28**, 482–488, DOI 10.1016/j.tree.2013.04.003 (2013).

19. H. Liu, Q. Ye, J. J. Wiens, Climatic-niche evolution follows similar rules in plants and animals. *Nature Ecology & Evolution* **4**, 753–763, DOI 10.1038/s41559-020-1158-x (2020).

20. J. M. Bennett *et al.*, The evolution of critical thermal limits of life on Earth. *Nature Communications* **12**, 1198, DOI 10.1038/s41467-021-21263-8 (2021).

21. M. M. Joachimski *et al.*, Five million years of high atmospheric CO2 in the aftermath of the Permian-Triassic mass extinction. *Geology* **50**, 650–654, DOI 10.1130/G49714.1 (2022).

22. Y. Sun *et al.*, Lethally Hot Temperatures During the Early Triassic Greenhouse. *Science* **338**, 366–370, DOI 10.1126/science.1224126 (2012).

23. S. M. Jones, M. Hoggett, S. E. Greene, T. Dunkley Jones, Large Igneous Province thermogenic greenhouse gas flux could have initiated Paleocene-Eocene Thermal Maximum climate change. *Nature Communications* **10**, 5547, DOI 10.1038/s41467-019-12957-1 (2019).

24. F. A. McInerney, S. L. Wing, The Paleocene-Eocene Thermal Maximum: A Perturbation of Carbon Cycle, Climate, and Biosphere with Implications for the Future. *Annual Review of Earth and Planetary Sciences* **39**, 489–516, DOI 10.1146/annurev-earth-040610-133431 (2011).

25. T. M. Lenton, S. J. Daines, B. J. Mills, COPSE reloaded: An improved model of biogeochemical cycling over Phanerozoic time. *Earth-Science Reviews* **178**, 1–28, DOI 10.1016/j.earscirev.2017.12.004 (2018).

26. T. Jezkova, J. J. Wiens, Rates of change in climatic niches in plant and animal populations are much slower than projected climate change. *Proceedings of the Royal Society B: Biological Sciences* **283**, 20162104, DOI 10.1098/rspb.2016.2104 (2016).

27. Z. Lososová *et al.*, Seed dispersal distance classes and dispersal modes for the European flora. *Global Ecology and Biogeography* **32**, 1485–1494, DOI 10.1111/geb.13712 (2023).

28. S. V. Sobolev *et al.*, Linking mantle plumes, large igneous provinces and environmental catastrophes. *Nature* **477**, 312–316, DOI 10.1038/nature10385 (2011).

29. H. Svensen *et al.*, Siberian gas venting and the end-Permian environmental crisis. *Earth and Planetary Science Letters* **277**, 490–500, DOI 10.1016/j.epsl.2008.11.015 (2009).

30. M. Capriolo *et al.*, Deep CO_2 in the end-Triassic Central Atlantic Magmatic Province. *Nature Communications* **11**, 1670, DOI 10.1038/s41467-020-15325-6 (2020).

31. M. Steinthorsdottir, A. J. Jeram, J. C. McElwain, Extremely elevated CO_2 concentrations at the Triassic/Jurassic boundary. *Palaeogeography, Palaeoclimatology, Palaeoecology* **308**, 418–432, DOI 10.1016/j.palaeo.2011.05.050 (2011).

32. C. J. Hollis *et al.*, The DeepMIP contribution to PMIP4: methodologies for selection, compilation and analysis of latest Paleocene and early Eocene climate proxy data, incorporating version 0.1 of

the DeepMIP database. *Geoscientific Model Development* **12**, 3149–3206, DOI 10.5194/gmd12-3149-2019 (2019).

33. M. Gutjahr *et al.*, Very large release of mostly volcanic carbon during the Palaeocene–Eocene Thermal Maximum. *Nature* **548**, 573–577, DOI 10.1038/nature23646 (2017).

34. M. Storey, R. A. Duncan, C. C. Swisher, Paleocene-Eocene Thermal Maximum and the Opening of the Northeast Atlantic. *Science* **316**, 587–589, DOI 10.1126/science.1135274 (2007).

35. T. S. Tobin, C. M. Bitz, D. Archer, Modeling climatic effects of carbon dioxide emissions from Deccan Traps volcanic eruptions around the Cretaceous–Paleogene boundary. *Palaeogeography, Palaeoclimatology, Palaeoecology* **478**, 139–148, DOI 10.1016/j.palaeo.2016.05.028 (2017).

36. R. A. Berner, Examination of hypotheses for the Permo–Triassic boundary extinction by carbon cycle modeling. *Proceedings of the National Academy of Sciences* **99**, 4172–4177, DOI 10.1073/pnas.032095199 (2002).

37. A. Grard, L. Francois, C. Dessert, B. Dupre, Y. Godderis, Basaltic volcanism and mass extinction at the Permo-Triassic boundary: Environmental impact and modeling of the global carbon cycle. *Earth and Planetary Science Letters* **234**, 207–221, DOI 10.1016/j.epsl.2005.02.027 (2005).

38. Y. Cui, L. R. Kump, Global warming and the end-Permian extinction event: Proxy and modeling perspectives. *Earth-Science Reviews* **149**, 5–22, DOI 10.1016/j.earscirev.2014.04. 007 (2015).

39. M. Capriolo *et al.*, Anthropogenic-scale CO_2 degassing from the Central Atlantic Magmatic Province as a driver of the end-Triassic mass extinction. *Global and Planetary Change* **209**, 103731, DOI 10.1016/j.gloplacha.2021.103731 (2022).

40. J. C. McElwain, S. W. Punyasena, Mass extinction events and the plant fossil record. *Trends in Ecology & Evolution* **22**, 548–557, DOI 10.1016/j.tree.2007.09.003 (2007).

41. D. H. Erwin, Lessons from the past: Biotic recoveries from mass extinctions. *Proceedings of the National Academy of Sciences* **98**, 5399–5403, DOI 10.1073/pnas.091092698 (2001).

42. C. V. Looy, W. A. Brugman, D. L. Dilcher, H. Visscher, The delayed resurgence of equatorial forests after the Permian–Triassic ecologic crisis. *Proceedings of the National Academy of Sciences* **96**, 13857–13862, DOI 10.1073/pnas.96.24.13857 (1999).

43. C. V. Looy, R. J. Twitchett, D. L. Dilcher, J. H. A. Van Konijnenburg-Van Cittert, H. Visscher, Life in the end-Permian dead zone. *Proceedings of the National Academy of Sciences* **98**, 7879–7883, DOI 10.1073/pnas.131218098 (2001).

44. B. A. Black, L. T. Elkins-Tanton, M. C. Rowe, I. U. Peate, Magnitude and consequences of volatile release from the Siberian Traps. *Earth and Planetary Science Letters* **317-318**, 363–373, DOI 10.1016/j.epsl.2011.12.001 (2012).

45. B. A. Black *et al.*, Systemic swings in end-Permian climate from Siberian Traps carbon and sulfur outgassing. *Nature Geoscience* **11**, 949–954, DOI 10.1038/s41561-018-0261-y (2018).

46. M. A. Sephton, C. V. Looy, H. Brinkhuis, P. B. Wignall, J. W. De Leeuw, H. Visscher, Catastrophic soil erosion during the end-Permian biotic crisis. *Geology* **33**, 941, DOI 10.1130/G21784.1 (2005).

47. J. C. McElwain, M. E. Popa, S. P. Hesselbo, M. Haworth, F. Surlyk, Macroecological responses of terrestrial vegetation to climatic and atmospheric change across the Triassic/Jurassic boundary in East Greenland. *Paleobiology* **33**, 547–573, DOI 10.1666/06026.1 (2007).

48. S. L. Wing *et al.*, Transient Floral Change and Rapid Global Warming at the Paleocene-Eocene Boundary. *Science* **310**, 993– 996, DOI 10.1126/science.1116913 (2005).

49. C. Jaramillo *et al.*, Effects of Rapid Global Warming at the Paleocene-Eocene Boundary on Neotropical Vegetation. *Science* **330**, 957–961, DOI 10.1126/science.1193833 (2010).

50. M. P. D'Antonio, D. E. Ibarra, C. K. Boyce, Land plant evolution decreased, rather than increased, weathering rates. *Geology* **48**, 29–33, DOI 10.1130/G46776.1 (2020).

51. B. J. W. Mills, S. Tennenbaum, D. Schwartzman, Exploring multiple steady states in Earth's longterm carbon cycle. *American Journal of Science* **321**, 1033–1044, DOI 10.2475/07.2021.01 (2021).

52. Y. Donnadieu, Y. Godderis, N. Bouttes, Exploring the climatic impact of the continental vegetation on the Mezosoic atmospheric CO_2 and climate history. *Clim. Past* **5**, 85–96, DOI 10.5194/cp-5-85-2009 (2009).

53. E. J. Judd *et al.*, The PhanSST global database of Phanerozoic sea surface temperature proxy data. *Scientific Data* **9**, 753, DOI 10.1038/s41597-022-01826-0 (2022).

54. C. Scotese, N. Wright, PALEOMAP Paleodigital Elevation Models (PaleoDEMS) for the Phanerozoic. Available from: https://www.earthbyte.org/paleodem-resource-scotese-and-wright-2018 (2018).

55. E. O. Straume, C. Gaina, K.H. Nisancioglu, Global Cenozoic Paleobathymetry with a focus on the Northern Hemisphere Oceanic Gateways. *Gondwana Research* **86**, 126–143, DOI 10.1016/j.gr.2020.05.011 (2020).

56. E. J. Judd *et al.*, Data for: PhanSST - A global database of Phanerozoic sea surface temperature proxy data, v0.0.1-beta, Zenodo (2022); https://doi.org/10.5281/zenodo.7275402.

57. J. Rogger *et al.*, Data and code for: Bio-geographic climate sensitivity controls Earth system response to Large Igneous Province carbon degassing, Zenodo (2024); https://doi.org/10.5281/zenodo.12187757.

58. O. Hagen *et al.*, gen3sis: A general engine for eco-evolutionary simulations of the processes that shape Earth's biodiversity. *PLOS Biology* **19**, e3001340, DOI 10.1371/journal.pbio.3001340 (2021).

59. M. Huang *et al.*, Air temperature optima of vegetation productivity across global biomes. *Nature Ecology & Evolution* **3**, 772–779, DOI 10.1038/s41559-019-0838-x (2019).

60. M. J. Donoghue, E. J. Edwards, Biome shifts and niche evolution in plants. *Annual Review of Ecology, Evolution, and Systematics* **45**, 547–572, DOI 10.1146/annurev-ecolsys-120213091905 (2014).

61. H. E. Beck *et al.*, Present and future Koppen-Geiger climate classification maps at 1-km resolution. *Scientific Data* **5**, 180214, DOI 10.1038/sdata.2018.214 (2018).

62. A. Takeshima *et al.*, Global aridity changes due to differences in surface energy and water balance between 1.5°C and 2°C warming. *Environmental Research Letters* **15**, 0940a7, DOI 10.1088/1748-9326/ab9db3 (2020).

63. J. M. J. Travis *et al.*, Modelling dispersal: an eco-evolutionary framework incorporating emigration, movement, settlement behaviour and the multiple costs involved. *Methods in Ecology and Evolution* **3**, 628–641, DOI 10.1111/j.2041-210X.2012.00193.x (2012).

64. W. Cramer *et al.*, Comparing global models of terrestrial net primary productivity (NPP): overview and key results. *Global Change Biology* **5**, 1–15, DOI 10.1046/j.1365-2486.1999.00009.x (1999).

65. M. J. Behrenfeld, P. G. Falkowski, Photosynthetic rates derived from satellite-based chlorophyll concentration. *Limnology and Oceanography* **42**, 1–20, DOI 10.4319/lo.1997.42.1.0001 (1997).

66. B. J. Mills, Y. Donnadieu, Y. Godderis, Spatial continuous integration of Phanerozoic global biogeochemistry and climate. *Gondwana Research* **100**, 73–86, DOI 10.1016/j.gr.2021.02.011 (2021).

67. A. J. West, Thickness of the chemical weathering zone and implications for erosional and climatic drivers of weathering and for carbon-cycle feedbacks. *Geology* **40**, 811–814, DOI 10.1130/G33041.1 (2012).

68. P. Maffre *et al.*, Mountain ranges, climate and weathering. Do orogens strengthen or weaken the silicate weathering carbon sink? *Earth and Planetary Science Letters* **493**, 174–185, DOI 10.1016/j.epsl.2018.04.034 (2018).

69. R. A. Berner, K. Caldeira, The need for mass balance and feedback in the geochemical carbon cycle. *Geology* **25**, 955–956, DOI 10.1130/0091-7613(1997)025<0955:TNFMBA>2.3.CO;2 (1997).

70. J. K. Caves, A. B. Jost, K. V. Lau, K. Maher, Cenozoic carbon cycle imbalances and a variable weathering feedback. *Earth and Planetary Science Letters* **450**, 152–163, DOI 10.1016/j.epsl.2016.06.035 (2016).

71. G. A. Shields, B. J. W. Mills, Tectonic controls on the long-term carbon isotope mass balance. *Proceedings of the National Academy of Sciences of the United States of America* **114**, 4318–43232, DOI 10.1073/pnas.1614506114 (2017).

72. R. Berner, A model for atmospheric CO_2 over Phanerozoic time. *American Journal of Science* **291**, 339–376, DOI 10.2475/ajs.291.4.339 (1991).

73. L. R. Kump, M. A. Arthur, Interpreting carbon-isotope excursions: carbonates and organic matter. *Chemical Geology* **161**, 181–198, DOI 10.1016/S0009-2541(99)00086-8 (1999).

74. Y. Donnadieu *et al.*, A GEOCLIM simulation of climatic and biogeochemical consequences of Pangea breakup. Geochemistry, Geophysics, Geosystems **7**, Q11019, DOI 10.1029/2006GC001278 (2006).

75. K. Fraedrich, A suite of user-friendly global climate models: Hysteresis experiments. *The European Physical Journal Plus* **127**, 53, DOI 10.1140/epjp/i2012-12053-7 (2012).

76. O. Mehling, K. Bellomo, M. Angeloni, C. Pasquero, J. Von Hardenberg, High-latitude precipitation as a driver of multicentennial variability of the AMOC in a climate model of intermediate complexity. *Climate Dynamics* **61**, 1519–1534, DOI 10.1007/s00382-022-06640-3 (2023).

77. D. O. Gough, Solar interior structure and luminosity variations. *Solar Physics* **74**, 21–34 (1981).

78. E. Pucéat *et al.*, Revised phosphate–water fractionation equation reassessing paleotemperatures derived from biogenic apatite. *Earth and Planetary Science Letters* **298**, 135–142, DOI 10.1016/j.epsl.2010.07.034 (2010).

79. S.-T. Kim, J. R. O'Neil, Equilibrium and nonequilibrium oxygen isotope effects in synthetic carbonates. *Geochimica et Cosmochimica Acta* **61**, 3461–3475, DOI 10.1016/S0016-7037(97)00169-5 (1997).

80. M. Daëron *et al.*, Most Earth-surface calcites precipitate out of isotopic equilibrium. *Nature Communications* **10**, 429, DOI 10.1038/s41467-019-08336-5 (2019).

81. L. Grossman, T.-L. Ku, Oxygen and carbon isotope fractionation in biogenic aragonite: temperature effects. *Chemical Geology* **59**, 59–74 (1986).

82. S. B. Malevich, L. Vetter, J. E. Tierney, Global core top calibration of ^{18}O in planktic foraminifera to sea surface temperature. *Paleoceanography and Paleoclimatology* **34**, 1292–1315, DOI 10.1029/2019PA003576 (2019).

83. J. E. Tierney, M. P. Tingley, A Bayesian, spatially-varying calibration model for the TEX$_{86}$ proxy. *Geochimica et Cosmochimica Acta* **127**, 83–106, DOI 10.1016/j.gca.2013.11.026 (2014).

84. J. E. Tierney, S. B. Malevich, W. Gray, L. Vetter, K. Thirumalai, Bayesian calibration of the Mg/Ca paleothermometer in planktic foraminifera. *Paleoceanography and Paleoclimatology* **34**, 2005–2030, DOI 10.1029/2019PA003744 (2019).

85. M. Schobben *et al.*, Latest Permian carbonate carbon isotope variability traces heterogeneous organic carbon accumulation and authigenic carbonate formation. *Climate of the Past* **13**, 1635–1659, DOI 10.5194/cp-13-1635-2017 (2017).

86. T. Westerhold *et al.*, Astronomical calibration of the Ypresian timescale: implications for seafloor spreading rates and the chaotic behavior of the solar system? *Climate of the Past* **13**, 1129–1152, DOI 10.5194/cp-13-1129-2017 (2017).

87. T. Westerhold, U. Rohl, B. Donner, J. C. Zachos, Global extent of early Eocene hyperthermal events: A new Pacific benthic foraminiferal isotope record from Shatsky Rise (ODP Site 1209). *Paleoceanography and Paleoclimatology* **33**, 626–642, DOI 10.1029/2017PA003306 (2018).

Acknowledgments: All model simulations were conducted on the ETH Zurich computer cluster 'Euler'. The authors thank Melissa Dawes for English editing.

Funding: This work was supported by the Swiss National Science Foundation grant 192296 (to JR, TVG, and LP) and the UK Research and Innovation projects EP/Y008790/1 and NE/X011208/1 (to BJWM).

Author contributions:

Conceptualization: JR, EJJ, BJWM, YG, TVG, LP

Software: JR

Formal Analysis: JR, EJJ

Supervision: TVG, LP

Validation: JR, EJJ, BJWM, YG, TVG, LP

Investigation: JR, EJJ

Visualization: JR, EJJ

Methodology: JR, EJJ, BJWM, YG, TVG, LP

Writing - original draft: JR, EJJ, BJWM, YG, TVG, LP

Writing review & editing: JR, EJJ, BJWM, YG, TVG, LP

Funding acquisition: TVG, LP

Competing interests: Authors declare that they have no competing interests.

Data and materials availability: All data sources are available in the manuscript or the Supplementary Material. Proxy data for the paleotemperature estimations are available at Zenodo (56), with further details described in (53). Model and analysis code are available at Zenodo (57).

Supplementary Materials

Materials and Methods
Figs. S1 to S13
References (58-87)

Supplementary Materials for

Bio-geographic climate sensitivity controls Earth system response to Large Igneous Province carbon degassing

Julian Rogger, Emily J. Judd, Benjamin J.W. Mills, Yves Goddéris, Taras V. Gerya, Loïc Pellissier

Corresponding author: julian.rogger@erdw.ethz.ch

The PDF file includes:

Materials and Methods
Figs. S1 to S13
References (58-87)

Materials and Methods

Model description

The model consists of three coupled components: an eco-evolutionary vegetation model, a geologic carbon cycle model, and a look-up structure of pre-run climate model simulations. Each presented climate trajectory represents a model run covering a time span of 8 Ma in time steps of 100 ka and at a spatial resolution of 3.75° × 3.75°.

Eco-evolutionary deep-time vegetation model. The eco-evolutionary vegetation model tracks vegetation primary productivity and vegetation-mediated enhancement of mineral weathering as a function of a flora's productivity and state of adaptation to the local environmental conditions. The developed vegetation model is based on *gen3sis* (*58*) (general engine for eco-evolutionary simulations), a framework designed to model various biological entities and their traits in a dynamic landscape, considering key processes such as dispersal, trait evolution and competition. In the present model configuration, a biological entity represents a terrestrial vegetation flora (assemblage of plants and symbiotic organisms living in a certain location at a certain point in time) that is characterized by two key characteristics also observed for present-day floras (*59*, *60*): a temperature niche and an aridity niche (niche for water availability). In the model, both characteristics are represented as a bell-shaped performance function around an optimum (T_{opt} for temperature and A_{opt} for aridity) for each model flora. T_{opt} and A_{opt} need to be understood as an ensemble response of all the organisms constituting a flora. The widths of the temperature and aridity niches are derived from bio-climatic classification systems that are often used to distinguish geographic regions with specific vegetation types (*61*). For the temperature niche, the width approximates the variation in mean annual temperatures observed within Koeppen-Geiger bio-climatic zones (approximately 10°C; fig. S1). For aridity, the niche width is approximated by the bin width of the Budyko aridity index (BAI) used to describe different hydroclimatic regions on the globe [BAI for humid: 0–1.2, semi-humid: 1.2–2, semi-arid: 2–4, arid: 4–6 (*62*); niche width of 2 BAI units used]. The BAI is defined as:

$$BAI = \frac{R_n}{\lambda \cdot P} \qquad (1)$$

where R_n is the net surface radiation, λ the latent heat of vaporization, and P the precipitation. Together, the temperature and aridity niche represent a geographic region in which a model flora can be productive. If the climate changes to conditions a flora is not adapted to, it is forced to adapt through migration and/or adaptive evolution of its niche.

The model is initialized with each terrestrial grid cell being occupied by an optimally adapted flora, with T_{opt} and A_{opt} corresponding to the local temperature and aridity, respectively (the possibility of a non-optimal adaptation state at the onset of the LIP is illustrated in fig. S9). At each time step, floras can disperse to other terrestrial grid cells within a dispersal range that is newly drawn for each flora and at each time step from a right-skewed dispersal kernel defined by a Weibull distribution with shape parameter two and a varying scale parameter γ. The choice of the dispersal kernel accounts for the highly stochastic nature of dispersal (e.g., depending on vegetation characteristics, dispersal vectors or environmental conditions) as well as the generally high frequency of short-distance dispersal and low frequency of long-distance dispersal (*18*). By additionally scaling the dispersal distances according to the rate of a flora's primary productivity potential (NPP_{norm}, see eq. 11), we account for the various costs associated with the process of reproduction and dispersal, giving higher chances for long-distance dispersal to well adapted and productive floras (*63*). In the presented parameter exploration (e.g., figs 1 & 2), we vary the scale parameter γ of the dispersal kernel within a range of 0–100'000 km Ma^{-1} (a multiple of Earth's circumference; considered unlimited dispersal) across the different simulations, covering a large range of empirically estimated plant dispersal abilities (unassisted dispersal: 0–5 m per generation time, wind dispersal: 2–500 m, animals as dispersal vector: 400–1500 m) (*18*, *27*). Changing the global dispersal kernel scale parameter allows us to test the effect of a globally low to high ability of vegetation floras to respond to climatic changes by dispersal, while maintaining the skewed nature of dispersal events.

In addition to dispersal-based adaptation, at every time step, a flora's T_{opt} and A_{opt} traits evolve *in situ* towards local environmental conditions at a varying prescribed maximum adaptation rate (θ for temperature and α for aridity), representing adaptive evolutionary processes. Climatic niche adaptation is the result of multiple processes that are interdependent and that act on different spatiotemporal scales, ranging from phenotypic plasticity, to changes in species composition, to actual evolutionary innovation (*60*). The speed at which species and entire floras can adapt to new climatic conditions is associated with large uncertainty (*19*, *20*, *26*). We thus test a large range of flora climatic niche adaptation rates, ranging from very slow (highly conserved climatic niche) to near-immediate adaptation. For temperature adaptation, we vary θ from 0–10°C Ma^{-1} between simulations, covering the empirical uncertainty range (*19*, *20*, *26*). Regarding aridity adaptation, we vary α from 0 to 100 Budyko units Ma^{-1} with the upper end-member representing a vegetation response that is not limited by aridity.

After dispersal and adaptation, a competition scheme determines the best-adapted flora that will ultimately occupy a terrestrial grid cell. For this scheme, a performance function (Ω) captures the degree of adaptation of each flora in each grid cell, considering the deviation of a flora's T_{opt} and A_{opt} to local climatic conditions as follows:

$$\Omega = T_{adaptation} \cdot A_{adaptation} \qquad (2)$$

$$T_{adaptation} = exp\left(-\beta_T \cdot \left(T_{opt} - T_{local}\right)^2\right) \tag{3}$$

$$A_{adaptation} = exp\left(-\beta_A \cdot \left(A_{opt} - A_{local}\right)^2\right) \tag{4}$$

where T_{local} and A_{local} are the grid cell's temperature and the local BAI, and β_T and β_A are the penalty parameters describing the performance of a flora for a given deviation of temperature and aridity from the flora's optimum (for the previously described niche width of approximately 10°C and 2 BAI units, the parameters are fixed at 0.1 and 5 for temperature and aridity, respectively). In addition to flora extinction due to competition, floras are assumed to die out if the prevailing temperature differs from the temperature niche by more than 15°C or if the prevailing aridity differs by more than 5 BAI units from the flora's niche, to avoid unrealistically large climate niche deviations. When combined, the modelled eco-evolutionary processes depict the vegetation response to a climatic change and how it varies depending on the vegetation's dispersal and adaptive evolution capacity. To assess the sensitivity of the global post-LIP climate evolution to the vegetation's ability to respond and adapt, the coupled carbon-climate-vegetation model is run for over 12,000 combinations of θ, α and γ.

Carbon cycling. At every time step, a model of the geologic carbon cycle tracks the carbon exchange between geologic reservoirs and the atmosphere-ocean carbon pool, from which atmospheric CO_2 and climate conditions are derived. The mass balance of the surface system is:

$$\frac{M_{AO}}{dt} = F_{degassing} + F_{LIP} - F_{silw} - F_{locb} - F_{mocb} \tag{5}$$

where M_{AO} is the mass of carbon in the exogenic system, $F_{degassing}$ a background inorganic and organic carbon degassing rate, F_{LIP} the carbon injection due to LIP magmatic activity, F_{silw} the carbon burial due to silicate mineral weathering, F_{locb} the burial of terrestrially derived organic carbon, and F_{mocb} the burial of marine organic carbon.

Terrestrial organic carbon production is considered a function of a flora's state of adaptation to its local environment, as well as abiotic factors. A flora's net primary productivity (NPP) per time step is calculated as:

$$NPP = \epsilon^* \cdot RSS \cdot T_{lim} \cdot A_{lim} \cdot \Omega \tag{6}$$

ϵ^* is the radiation conversion efficiency, scaled to obtain a present-day land-derived organic carbon burial rate (F_{locb}) of about $3.5 \cdot 10^{12}$ mol C year^{-1} (*25*) with present-day climate and geographic boundary conditions and assuming a constant burial efficiency b_{eff} (0.0007) of NPP [$F_{locb} = b_{eff} \cdot NPP$, with b_{eff} derived from present day rates of NPP and organic carbon burial (*25*, *64*)]. RSS the surface net shortwave radiation. T_{lim} a temperature limitation factor that is 0 for mean annual temperatures lower than -10°C or higher than 55°C, 1 for temperatures between 0 and 45°C, and linearly interpolated for transition temperatures. A_{lim} the water limitation of productivity, expressed as a function of the local BAI:

$$A_{lim} = 1 - \frac{1}{1 + exp\big(-3 \cdot (BAI - 2)\big)} \tag{7}$$

A_{lim} is approximately 1 in humid zones (BAI: 0–1.2), 0.5 at the transition from semi-humid to semi-arid (BAI: 2), and 0 for arid to hyperarid regions (BAI: 4–6). Ω again represents the flora's state of adaptation and performance in local conditions. A comparison of modelled NPP rates with this simplified vegetation model and data-based estimates for the present day is shown in fig. S10.

Marine primary productivity is approximated using an empirically derived chlorophyll-normalized temperature dependence of photosynthetic productivity P_b^{opt} (65) that accounts for temperature-limited productivity at sea surface temperatures (SST) below 20°C and nutrient- or stratification-limited productivity at temperatures higher than 20°C. Further, ocean productivity is taken to be proportional to silicate weathering rates, assuming that silicate weathering on land is the main nutrient input (i.e., phosphorus) to the ocean (*66*):

$$NPP_{ocean} = \phi_{scale} \cdot P_b^{opt}(SST) \cdot \frac{F_{silw}}{F_{silw,0}} \tag{8}$$

where ϕ_{scale} is a scaling factor used to obtain a present-day F_{mocb} of $3.5 \cdot 10^{12}$ mol C year^{-1} (*25*), with present-day climatic and geographic boundary conditions and assuming a constant burial efficiency of NPP ($F_{mocb} = b_{eff} \cdot NPP_{ocean}$); F_{silw} the current time step's rate of continental silicate weathering; and $F_{silw,0}$ the initial rate of continental silicate weathering.

Following other deep-time biogeochemical models (*66*), silicate weathering is calculated using the approach by (*67*) where it is expressed as a function of local erosion, temperature and runoff:

$$\omega_{silw} = \chi_m \cdot \varepsilon \cdot \left(1 - exp\left[-K \cdot e^{\frac{E_a}{RT_0} - \frac{E_a}{RT}} \cdot (1 - e^{-k_w \cdot q}) \cdot \frac{(z/\varepsilon)^{\sigma+1}}{(\sigma + 1)}\right]\right) \cdot f_{NPP} \tag{9}$$

where ω_{silw} is the flux of cations released during silicate weathering. ε is the local erosion, calculated as a function of topographic slope (s), runoff (q) and a scale parameter k_e (calibrated to reproduce present day rates of erosion) (*68*):

$$\varepsilon = k_e \cdot q^{0.5} \cdot s \tag{10}$$

In Eq. 9, T is the local temperature, χ_m the cation abundance in the bedrock (0.1), z the regolith thickness (10 m), E_a the apparent activation energy of silicate weathering (20 kJ mol^{-1}), R the ideal gas constant and T_0 the standard temperature. K, k_w and σ are three calibration constants ($6 \cdot 10^{-5}$, $1 \cdot 10^{-3}$ and -0.1) [all adapted from (*66*)]. As in other geologic carbon cycle models, the weathering parameters are kept constant in all simulations due to the lack of detailed global lithologic information for the geologic past.

Finally, f_{NPP} in Eq. 9 is a weathering enhancement factor representing the local vegetation-mediated enhancement of mineral weathering as a function of the local flora's productivity and adaptation state. It is derived using a normalized vegetation productivity potential (NPP_{norm}, between 0 and 1):

$$NPP_{norm} = \frac{RSS}{RSS_{max}} \cdot T_{lim} \cdot A_{lim} \cdot \Omega \tag{11}$$

where RSS_{max} is 5000 MJ m^{-2} $year^{-1}$ (tropical radiation intensity), representing the threshold for non-radiation-limited photosynthesis.

Following (*25*), the vegetation-mediated enhancement is then calculated as:

$$f_{NPP} = \left[\left(1 - min(NPP_{norm}, 1)\right) \cdot PREPLANT \cdot RCO_2^{0.5} + NPP_{norm}\right] \tag{12}$$

where RCO_2 the ratio of the current atmospheric CO_2 concentration to the initial concentration, and $PREPLANT$ is the weathering efficiency in the absence of plants. The choice of $PREPLANT$ defines the difference in weathering enhancement between bare ground and vegetated land. We test two values for the $PREPLANT$ parameter, 1/4 (fig. 2) and 1/6 (fig. S3), which correspond to a maximum four-fold and a six-fold increase in weathering rates in areas with high plant primary productivity. The considered vegetation-mediated weathering enhancement corresponds to the range observed in laboratory and field studies and to the values used in other deep-time biogeochemical models (*9*, *10*, *12*, *25*).

The current timestep's rate of CO_2 consumption by silicate weathering is assumed to be proportional to the cation release ω_{silw} (*66*), with a present-day rate of carbon burial due to silicate weathering ($k_{silw,ref}$) of $1.0 \cdot 10^{13}$ mol C $year^{-1}$ (*25*) and a present-day cation release ($\omega_{silw,ref}$) calculated for the present-day topography and climate.

$$F_{silw} = k_{silw,ref} \cdot \frac{\omega_{silw}}{\omega_{silw,ref}} \tag{13}$$

The last carbon flux considered is the degassing of carbon from the solid Earth into Earth's atmosphere and ocean. $F_{degassing}$ denotes the background inorganic and organic carbon degassing from magmatism and volcanism. It is also assumed to include possible carbon contributions from oxidative weathering of organic carbon stored in rocks. Given that for a multi-million-year period, the geologic carbon cycle is assumed to be in a ± 5% balance between carbon source and sink fluxes (*69*, *70*), $F_{degassing}$ is set equal to all carbon sink fluxes ($F_{degassing} = F_{silw} + F_{locb} + F_{mocb}$) at the start of a simulation. During the first 800 kyr of the model period, only small fluctuations in degassing are imposed, with the variations drawn randomly from a normal distribution with a mean of 0 and a standard deviation of $1 \cdot 10^{11}$ mol C year^{-1}. This background rate of degassing is being emitted to the atmosphere-ocean carbon pool throughout the simulations. During the LIP phase, F_{LIP} represents the estimated carbon injection due to LIP magmatism. The duration and mass of degassing is varied according to estimated degassing potentials of the Siberian Traps (Permian–Triassic), the Central Atlantic Magmatic Province (Triassic–Jurassic) and the North Atlantic Igneous Province (Paleocene–Eocene) (see main article).

We test the effect of seafloor weathering CO_2 consumption as an additional carbon cycle feedback. Seafloor weathering is approximated following (*66*) as a global flux dependent on the global average surface temperature:

$$F_{sfw} = k_{sfw,ref} \cdot e^{0.0608 \cdot (T_{GAST} - 288)} \tag{14}$$

where $k_{sfw,ref}$ is a reference weathering rate of $1.75 \cdot 10^{12}$ mol C year^{-1} at a reference global average surface temperature of 288 K, and T_{GAST} is the current global average surface temperature. Additionally, we test the sensitivity of the results to a weaker CO_2-induced weathering enhancement in the absence of vegetation ($RCO_2^{0.3}$ instead of $RCO_2^{0.5}$ in Eq. 12). The results of these sensitivity tests are shown in fig. S11 for the Permian-Triassic paleogeographic configuration.

To obtain a first-order approximation of how the modelled changes in organic and inorganic carbon fluxes after a LIP degassing event affect the isotopic signature of buried carbonate carbon ($\delta^{13}C_{carb}$), we follow (*71*), assuming a steady state in the atmosphere-ocean $\delta^{13}C$ for a model time step larger than the residence time of carbon in the ocean (≈ 10^5 years):

$$\delta^{13}C_{in} = \delta^{13}C_{org} \cdot f_{org} + \delta^{13}C_{carb} \cdot \left(1 - f_{org}\right) \tag{15}$$

To derive the $\delta^{13}C$ of buried carbonate carbon, an average isotopic composition of degassed carbon $\delta^{13}C_{in}$ of −6‰ and an average isotopic composition of buried organic carbon $\delta^{13}C_{org}$ of −27‰ are assumed. Finally, f_{org} defines the ratio of total organic (marine + terrestrial) to total organic and inorganic (from silicate + carbonate weathering) carbon burial. While carbonate weathering affects the $\delta^{13}C$ balance, it is a CO_2-neutral process for long time scales (*72*) and therefore is not included in the atmosphere-ocean carbon balance. It is approximated following (*66*) and calculated based on spatial fields of runoff and biotic weathering enhancement as:

$$F_{carbw} = k_{carbw} \cdot q \cdot f_{NPP} \tag{16}$$

where k_{carbw} represents a scale parameter, included to obtain a present-day rate of carbonate weathering of $8 \cdot 10^{12}$ mol C year^{-1} with present-day topography and climate conditions (*66*). A comparison of modelled and observed carbonate $\delta^{13}C$ for the Permian-Triassic and the Paleocene-Eocene is shown in fig. S4.

Climate model. With the carbon cycle model, carbon fluxes in and out of the combined pool of Earth's atmosphere and oceans are tracked. Assuming a baseline atmosphere-ocean carbon mass M_{AO} of $3.193 \cdot 10^{18}$ mol C at a 280 ppm atmospheric CO_2 concentration (*25*), atmospheric CO_2 concentration is set to be proportional to the square of the total carbon in the atmosphere-ocean pool (*73*):

$$CO_{2,t} = CO_{2,0} \cdot \left(\frac{M_{AO,t}}{M_{AO,0}}\right)^2 \tag{17}$$

where $CO_{2,t}$ is the current and $CO_{2,0}$ the initial CO_2 concentration; $M_{AO,t}$ the current and $M_{AO,0}$ the initial atmosphere-ocean carbon content, respectively.

A full dynamic coupling of a climate model with the above-described vegetation and carbon cycle model is currently not feasible, first because of computational limitations (climate models integrate over periods of hundreds to several thousand years, not the multi-million-year periods considered here), and second, because standard vegetation models integrated into climate models do not include the eco-evolutionary dynamics considered here (i.e., dispersal and adaptation processes). To overcome this limitation, we follow an approach commonly used in geologic carbon cycle modelling (*66*, *74*), where climatic conditions at every model time step are interpolated from a lookup table of pre-run climate simulations. A quantification of the uncertainty in surface climatic conditions arising from implementing this interpolation routine instead of running a new climate model for each time step's atmospheric CO_2 concentration is illustrated in fig. S12. To create the climate lookup table, an Earth system model of intermediate complexity, PlaSim (*75*, *76*), is run for atmospheric CO_2 concentrations between 100 and 8000 ppm for each considered continental configuration (from 100 to 1000 ppm in 50 ppm steps, from 1125 to 3000 in 125 ppm steps, and from 3000 to 8000 in 500 ppm steps). For each studied period, the solar luminosity is adjusted following the solar physics model of Gough (*77*). PlaSim is run with a mixed-layer slab ocean model and thermodynamic sea ice. To avoid confounding effects with vegetation models that can be coupled to PlaSim, the climate model is run without dynamic vegetation, with a uniform surface albedo on land (0.2), and with a constant soil depth (0.15 m). For each atmospheric CO_2 concentration, PlaSim is run for 250 model years, using the average temperature, precipitation, runoff and radiation of the last 50 model years to inform the eco-evolutionary vegetation model and the carbon cycle processes explained above. The continental configurations for the PlaSim simulations, as well as the other model components, are taken from (*54*) (maps for Permian-Triassic, Triassic-Jurassic and present) and from (*55*) for the Paleocene-Eocene and are assumed to be fixed for the entire 8 Ma model period. It should be noted that, as we do not fully integrate the studied vegetation dynamics into the PlaSim climate model, we can only consider the effects of eco-evolutionary vegetation on climate through changes in the atmosphere-ocean carbon content, and not through direct interactions with the climate system, including changes to surface albedo, water and energy exchange.

Paleotemperature proxies

The records documenting the sea surface temperature changes ($\Delta SST_{composite}$) across the Permian– Triassic, Triassic–Jurassic, and Paleocene–Eocene boundaries (Fig. 2) are compiled using proxy data from the PhanSST database (*53*). For each time slice, we utilize data from the chronostratigraphic stage (i.e., geochronologic age) preceding the LIP-associated boundary and the two to three stages postdating the boundary. The Ypresian (Eocene) is subdivided into three equal time bins (sub-stages) due to its extended duration, high data density, and reliable age control (*53*), and the PETM data are further subdivided following (*32*).

For each of the three boundaries, we isolate records from the same site and proxy system that have unaltered data from at least two of the (sub-)stages, following the diagenetic screening protocol of (*53*). This results in 15 unique records for the Permian–Triassic transition (14 $\delta^{18}O_{phosphate}$ and one $\delta^{18}O_{carbonate}$), 11 records for the Triassic–Jurassic (10 $\delta^{18}O_{carbonate}$, 1 TEX_{86}), and 36 records for the PETM (11 $\delta^{18}O_{carbonate}$, 14 TEX_{86}, and 11 Mg/Ca). Sample sites for each period are shown in fig. S13.

Sea surface temperatures (SSTs) are estimated from the proxy data using established transfer functions or proxy system models (*78*–*84*). Conodont $\delta^{18}O_{phosphate}$ data are brought into the same reference frame using an NBS-120c standard value of 21.7‰ and a Durango standard value of 9.8‰. Both BAYFOX (*82*) and BAYSPAR (*83*) are run using a prior mean value of 25°C and a prior standard deviation of 10°C. BAYMAG is run using a prior standard deviation of 10°C, the newest version of the seawater Mg/Ca curve (i.e., option 2 in BAYMAG), an H value of 0.75 (*84*), and an omega value of 5. With both BAYFOX and BAYMAG, we use the pooled species annual calibration. Estimating absolute SST from oxygen isotope data requires an assumption about the $\delta^{18}O$ value of the seawater (*78*–*82*), which is difficult to constrain in deep time. However, this assumption is negated when calculating SST differences between time intervals, provided that the seawater composition remained constant across any given record.

$\Delta SST_{composite}$ is estimated by subtracting the median pre-LIP SST of each record from each data point in that record. Not all records have data from the stage preceding the LIP-associated transition; in those instances, we use the median ΔSST of the subsequent (sub-)stage from the records with pre-LIP data to estimate a baseline ΔSST for each remaining record.

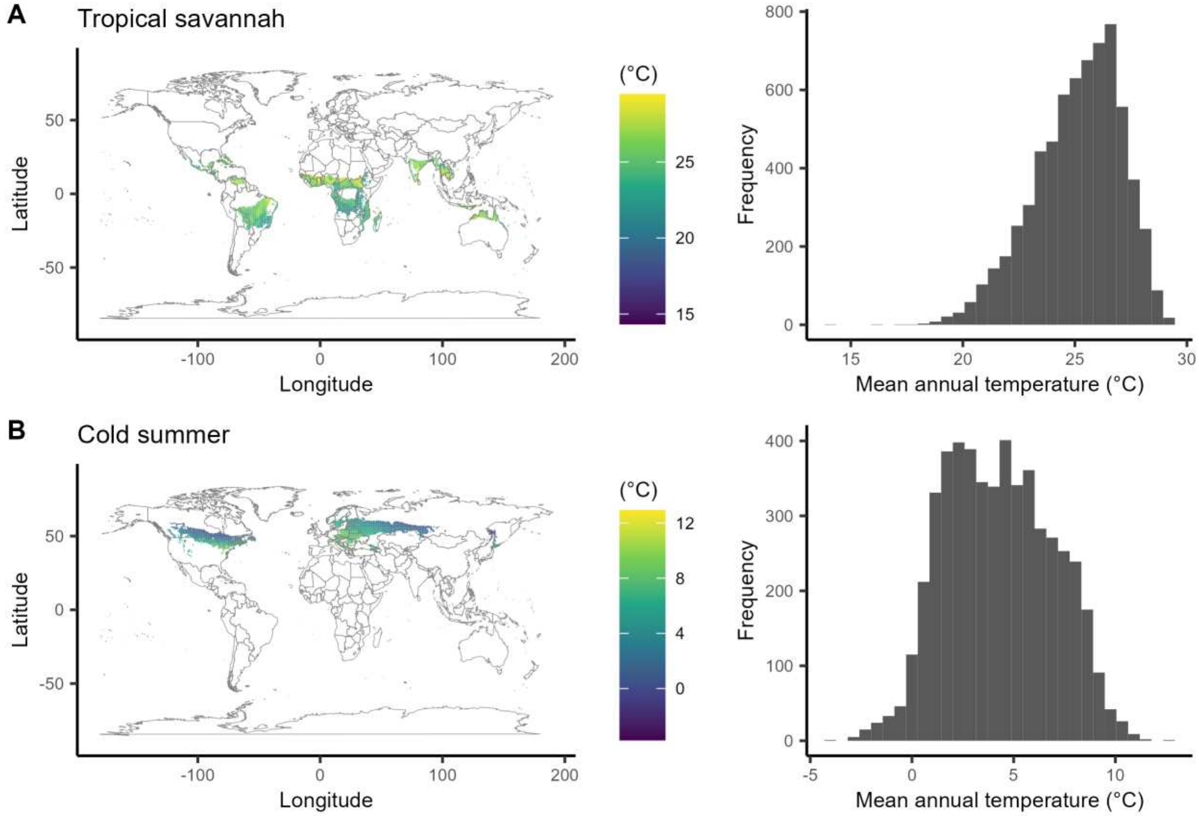

Fig. S1: Range of mean annual temperatures observed within Koeppen-Geiger vegetation zones. Location and temperature range within the **A.** tropical savannah and **B.** cold summer Koeppen-Geiger zone. Koeppen-Geiger zones are often used to distinguish among contrasting biological and climatic regions on Earth that are characterized by similar vegetation types. The range of mean annual temperatures observed within a Koeppen-Geiger zone is approximately 10°C, which is the temperature niche width used for the modelled floras. Data from (61).

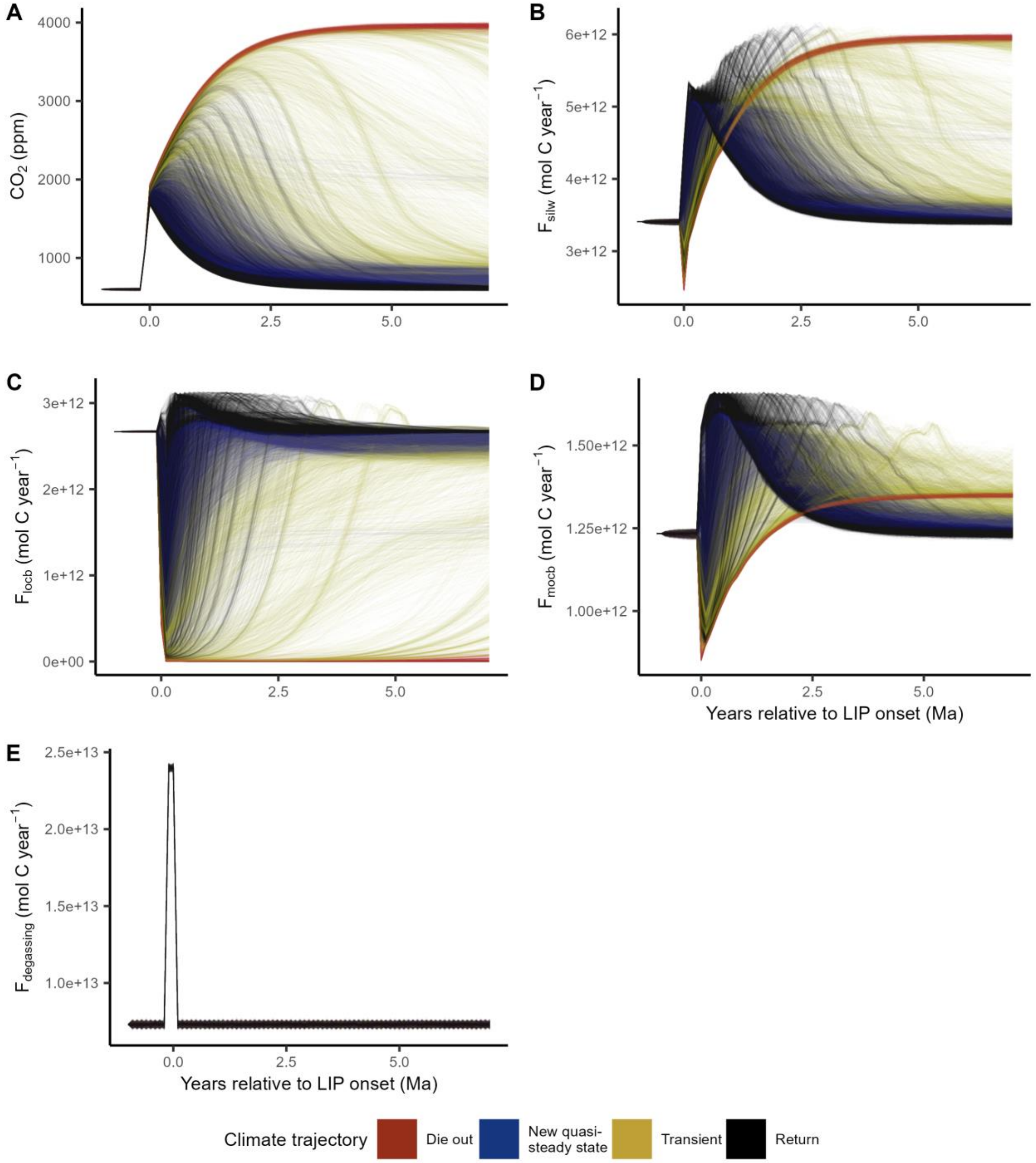

Fig. S2: Carbon flux dynamics for modelled range of climate trajectories observed for the Siberian Traps Large Igneous Province (Permian–Triassic transition). A. atmospheric CO$_2$ concentration, **B.** silicate weathering (F_{silw}), **C.** land-derived organic carbon burial (F_{locb}), **D.** marine organic carbon burial (F_{mocb}), **E.** carbon degassing (background + LIP) ($F_{degassing}$).

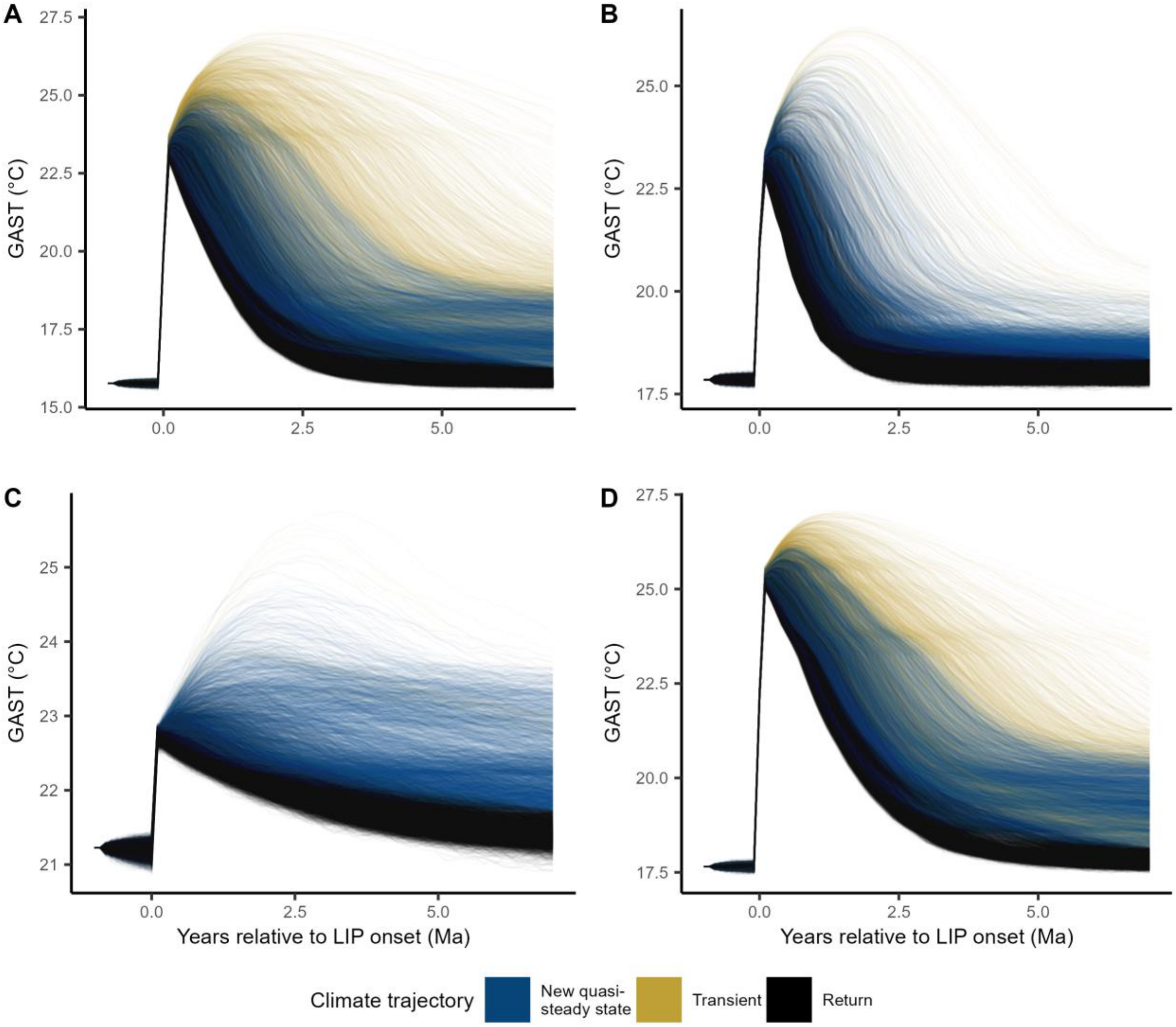

Fig. S3: Global average temperature (GAST) trajectories for an alternative set of model boundary conditions. A. Permian-Triassic configuration with an increased sensitivity of silicate weathering to plant primary productivity: maximum six-fold increase in weathering rates in highly productive areas compared with four-fold in the default configuration. **B.** Triassic-Jurassic configuration with an increased sensitivity of silicate weathering to plant primary productivity (maximum six-fold enhancement). **C.** Paleocene-Eocene configuration with a reduced carbon degassing mass of 8’000 Gt (instead of 15’000 in main the main text). **D.** Permian-Triassic configuration with a higher starting CO_2 concentration of 800 ppm (instead of 600 ppm in the main text) and a greater mass of carbon degassing of 50,000 Gt (instead of 40,000 Gt in the main text).

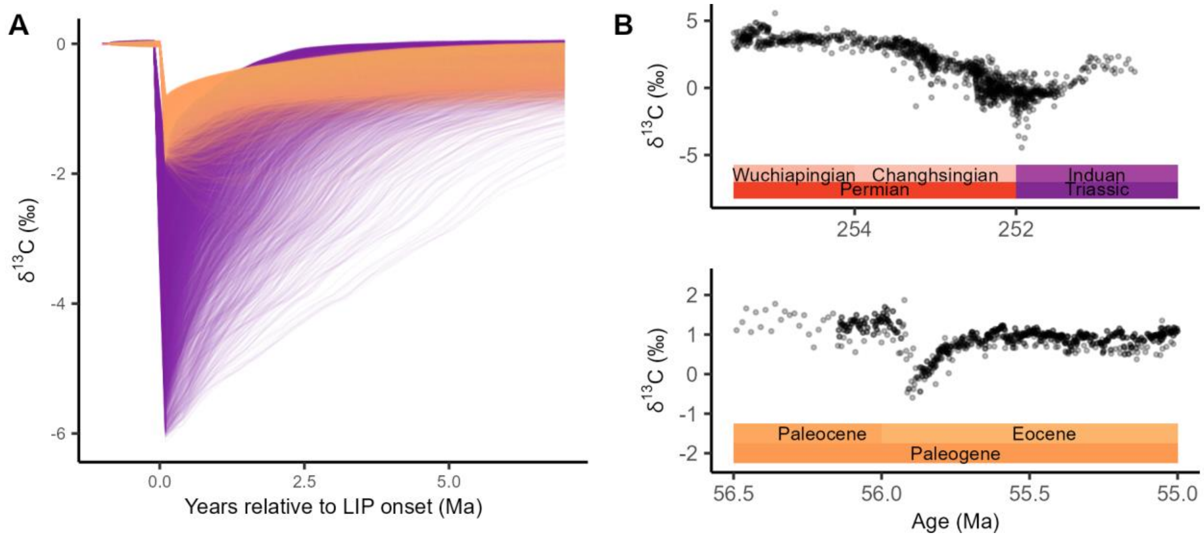

Fig. S4: Post-Large Igneous Province carbonate $\delta^{13}C$ dynamics. A. Modelled changes in the carbonate $\delta^{13}C$ record based on changes in organic and inorganic carbon burial. **B.** composite $\delta^{13}C$ curve over the Permian–Triassic boundary from various sources, as compiled in (*85*) (only Iran sections shown), and benthic $\delta^{13}C$ data over the Paleocene–Eocene boundary from ODP sites 1209, 1262 and 1263 from various sources, as compiled in (*86*, *87*).

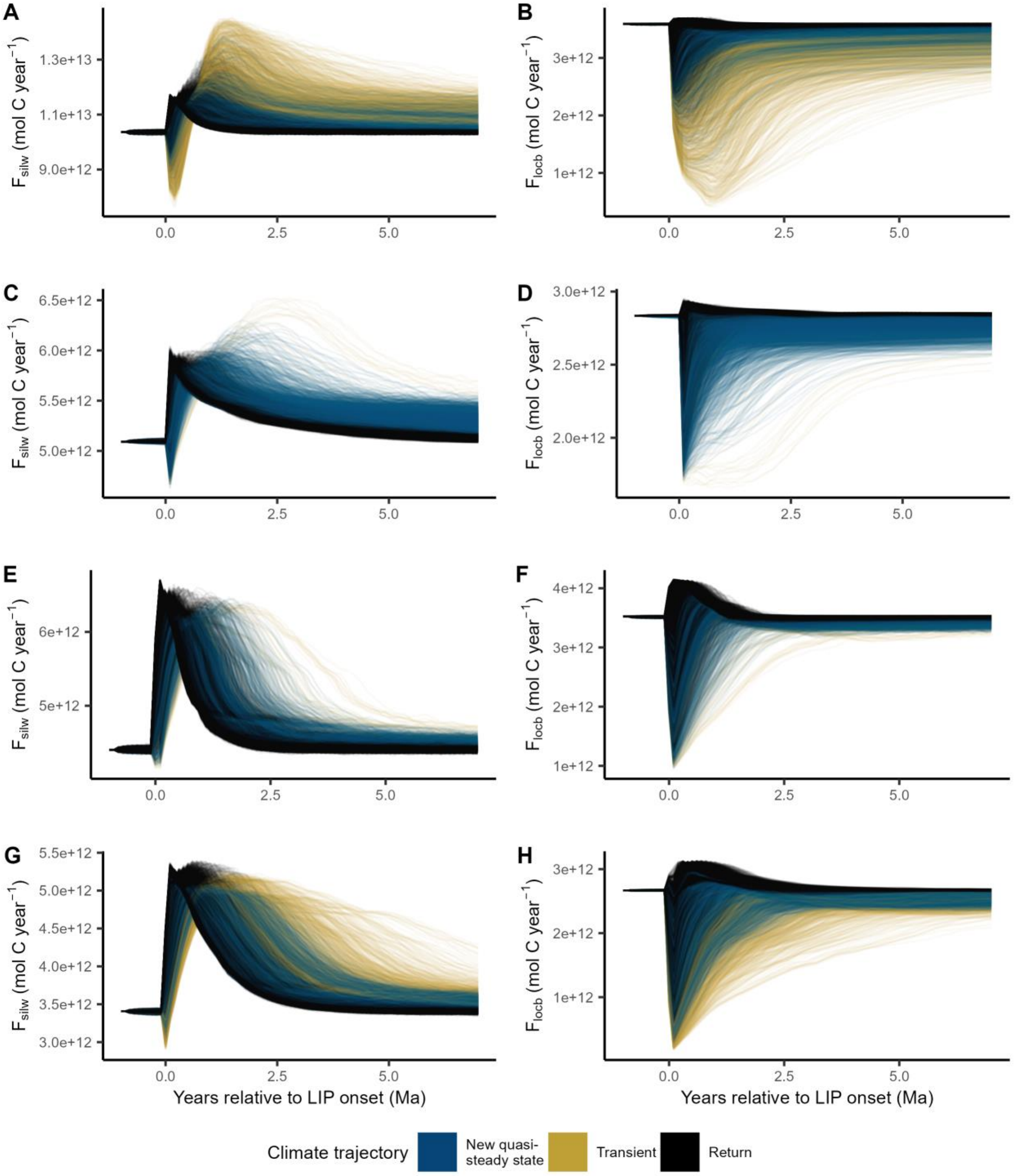

Fig. S5: Carbon burial fluxes for the modelled Phanerozoic Large Igneous Province (LIP) degassing events. Silicate weathering (F_{silw}; left column) and land-derived organic carbon burial (F_{locb}; right column) for the present-day hypothetical LIP (**A.** & **B.**), the North Atlantic Igneous Province (Paleocene-Eocene) (**C.** & **D.**), the Central Atlantic Igneous Province (Triassic-Jurassic) (**E.** & **F.**), and the Siberian Traps (Permian-Triassic) (**G.** & **H.**).

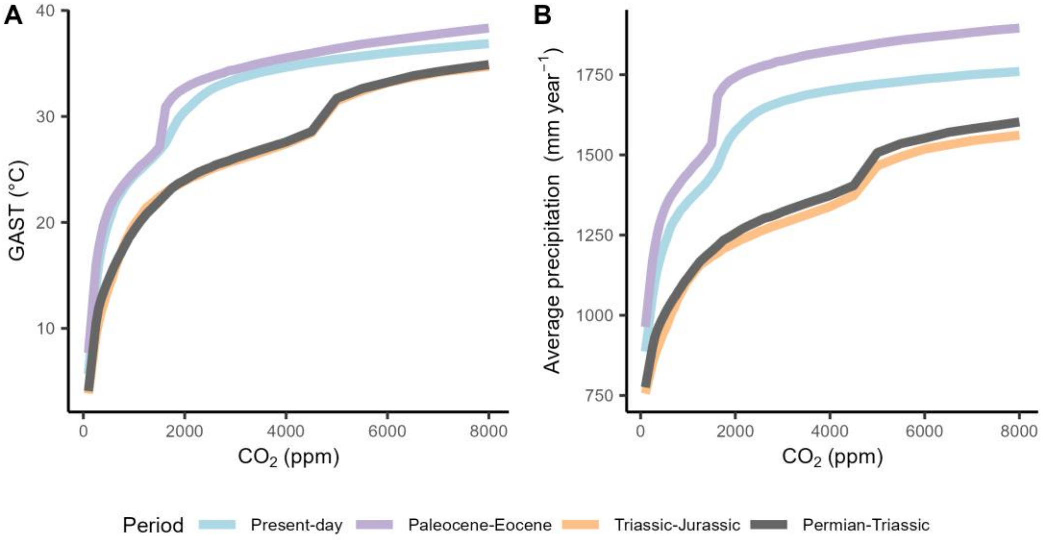

Fig. S6: Modelled climate sensitivity. A. Sensitivity of global average surface temperature (GAST) and **B.** global average precipitation to an increase in atmospheric CO_2 concentration as observed in the PlaSim climate simulations for the Permian-Triassic, Triassic-Jurassic, Paleocene-Eocene and present-day continental configurations.

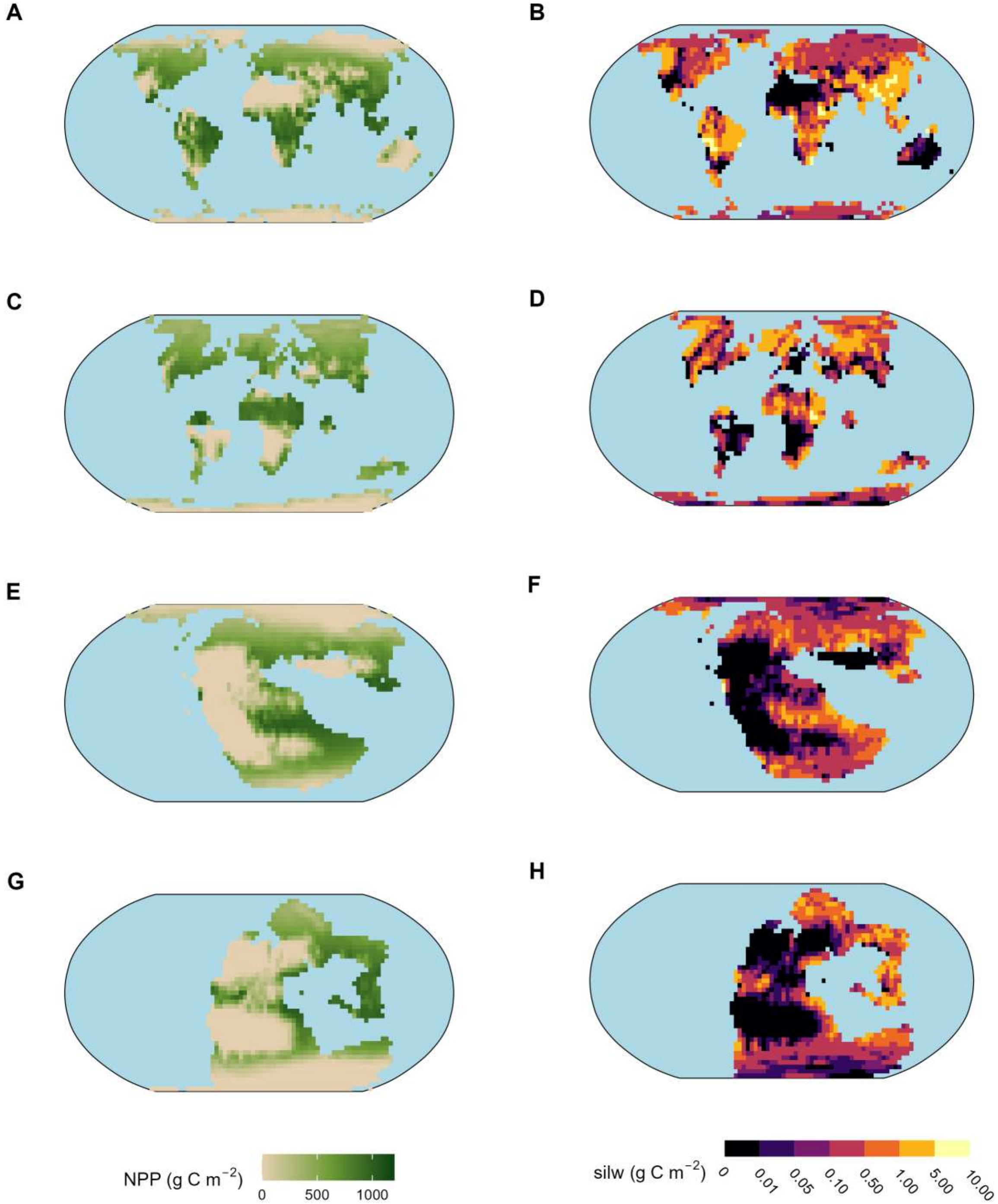

Fig. S7: Spatial distribution of net primary productivity (NPP) and silicate weathering carbon consumption. NPP (left column) and silicate weathering (silw; right column) for the present-day continental configuration (**A.** & **B.**), for the Paleocene-Eocene continental configuration (**C.** & **D.**), for the Triassic-Jurassic continental configuration (**E.** & **F.**), and for the Permian-Triassic continental configuration (**G.** & **H.**). Paleogeographic reconstructions are from (*55*) for the Paleocene-Eocene and otherwise from (*54*). Note that in the model, only a small fraction of NPP ultimately becomes buried (F_{locb}). Note also the uneven color scale for silicate weathering.

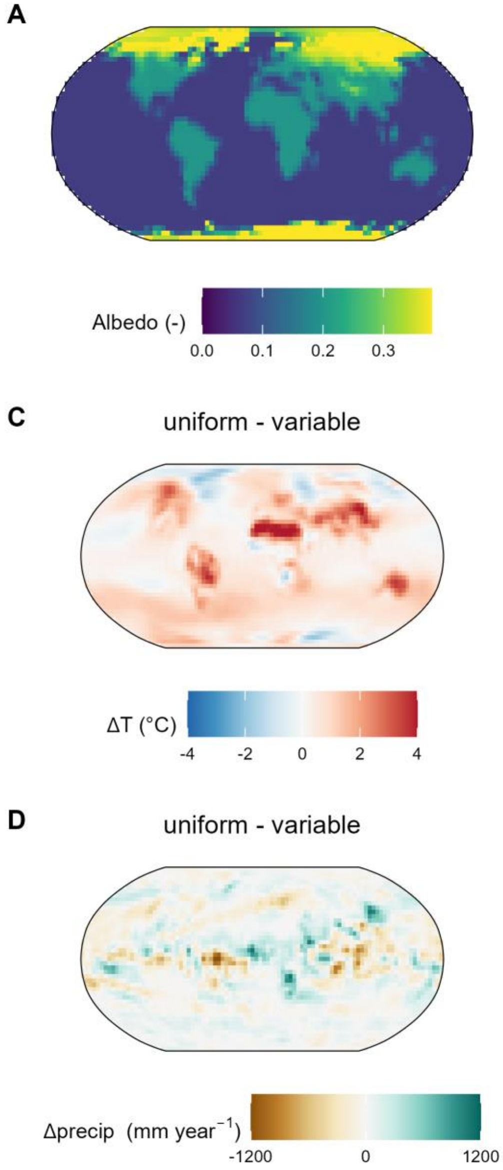

Fig. S8: Surface albedo-induced climate change. A. Uniform surface albedo of 0.2 on snow- and ice-free land. **B.** Example PlaSim climate simulation with an altered surface albedo scheme: higher surface background albedo of 0.25 and lower albedo only in areas with a potentially high vegetation cover as estimated by the PlaSim model. **C.** Difference in surface temperature between uniform and variable albedo scheme. If LIP-triggered vegetation shifts result in the exposure of surfaces of higher or lower albedo, a cooling or a warming effect on regional and global climate can be expected, respectively. **D.** Difference in annual precipitation between uniform and variable albedo scheme.

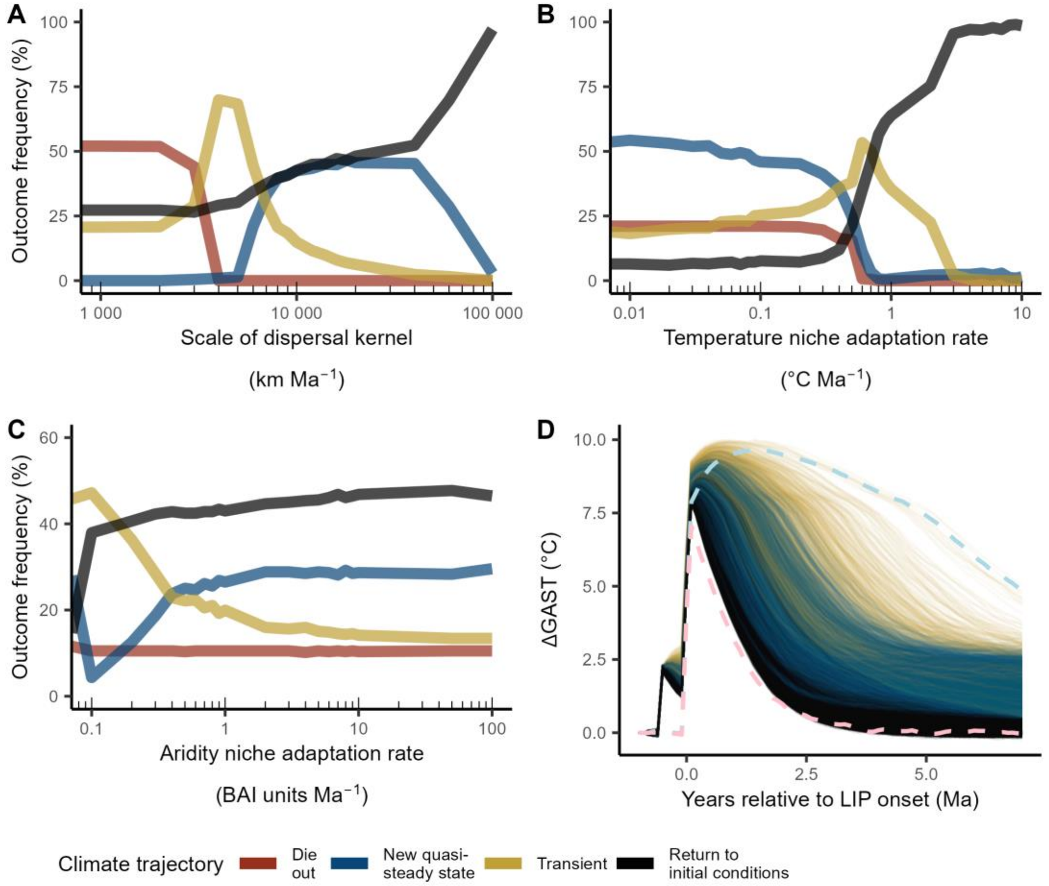

Fig. S9: Model results for pre-perturbed vegetation at onset of Large Igneous Province (LIP) degassing. This is achieved by imposing a carbon cycle perturbation before the onset of the LIP, resulting in non-optimally-adapted vegetation floras. Classification of the model outcome depending on **A.** the vegetation's dispersal capacity, **B.** the temperature niche adaptation rate, and **C.** the aridity niche adaptation rate. Model outcome frequencies are similar to the results presented in the main text, but with slightly more 'transient' trajectories that did not reach a steady state at the end of the simulation. **D.** Range of climate trajectories for a reduced biological parameter set (excluding 'die-out' trajectories and assuming non-zero temperature and aridity niche adaptation rates). For reference, the fast (pink) and slow (blue) vegetation adaptation end-member trajectories of the model presented in the main text are displayed.

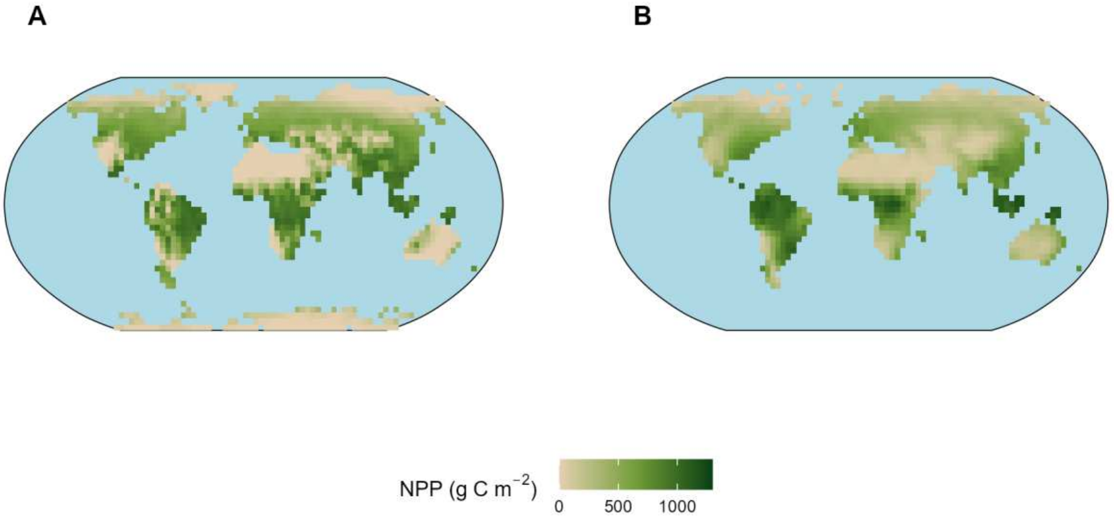

Fig. S10: Validation of modelled net primary productivity (NPP). A. NPP modelled using the developed deep-time vegetation model and climate input data from the intermediate-complexity climate model PlaSim (CO_2 concentration of 400 ppm, resolution 3.75°× 3.75°; averaged over 50 model years) and topographic data from (*54*). **B.** NPP estimate by (*64*) using monthly average climate data from 1931 to 1961 (ensemble mean of 17 estimates derived from vegetation models and satellite data; resampled to the resolution of the eco-evolutionary vegetation model for comparison).

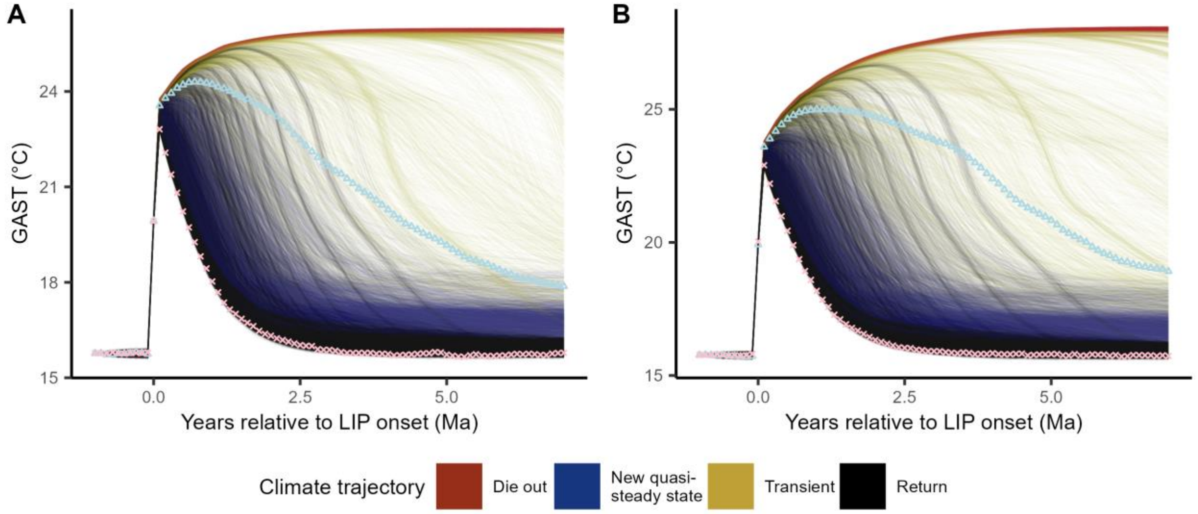

Fig. S11: Sensitivity of global average surface temperature trajectories (GAST) to carbon cycle feedback mechanisms. A. Permian-Triassic simulation with seafloor weathering feedback. **B.** Permian-Triassic simulation with seafloor weathering feedback but a weaker CO_2-dependent weathering feedback in the absence of plants or in locations of reduced primary productivity ($RCO_2^{0.3}$ instead of $RCO_2^{0.5}$ in Eq. 12).

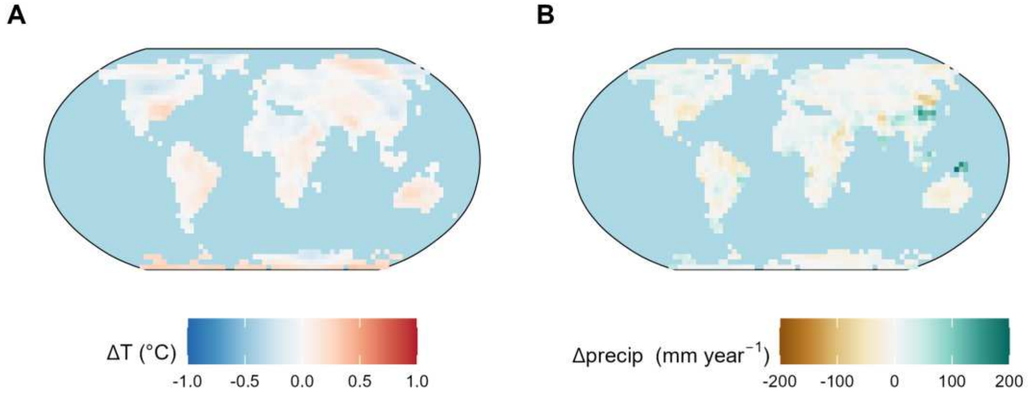

Fig. S12: Uncertainty in surface climatic conditions due to the climate interpolation routine. Plots depict the difference in **A.** surface temperature and **B.** precipitation between an interpolated climate for 800 ppm (interpolated from climate runs for 850 and 750 ppm) and an actual climate model output for 800 ppm.

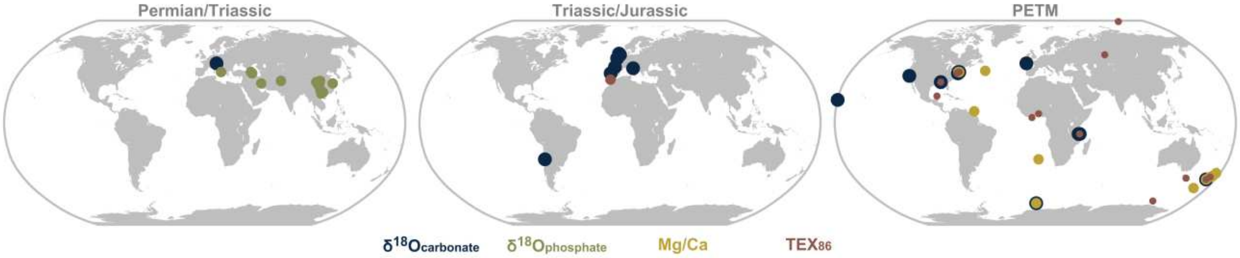

Fig. S13: Sampling sites of paleotemperature proxies. Locations of analyzed proxies for **A.** the Permian–Triassic transition **B.** the Triassic–Jurassic transition, and **C.** the Paleocene–Eocene transition.

References

58. O. Hagen *et al.*, gen3sis: A general engine for eco-evolutionary simulations of the processes that shape Earth's biodiversity. *PLOS Biology* **19**, e3001340, DOI 10.1371/journal.pbio.3001340 (2021).

59. M. Huang *et al.*, Air temperature optima of vegetation productivity across global biomes. *Nature Ecology & Evolution* **3**, 772–779, DOI 10.1038/s41559-019-0838-x (2019).

60. M. J. Donoghue, E. J. Edwards, Biome shifts and niche evolution in plants. *Annual Review of Ecology, Evolution, and Systematics* **45**, 547–572, DOI 10.1146/annurev-ecolsys-120213091905 (2014).

61. H. E. Beck *et al.*, Present and future Koppen-Geiger climate classification maps at 1-km resolution. *Scientific Data* **5**, 180214, DOI 10.1038/sdata.2018.214 (2018).

62. A. Takeshima *et al.*, Global aridity changes due to differences in surface energy and water balance between 1.5°C and 2°C warming. *Environmental Research Letters* **15**, 0940a7, DOI 10.1088/ 1748-9326/ab9db3 (2020).

63. J. M. J. Travis *et al.*, Modelling dispersal: an eco-evolutionary framework incorporating emigration, movement, settlement behaviour and the multiple costs involved. *Methods in Ecology and Evolution* **3**, 628–641, DOI 10.1111/j.2041-210X.2012.00193.x (2012).

64. W. Cramer *et al.*, Comparing global models of terrestrial net primary productivity (NPP): overview and key results. *Global Change Biology* **5**, 1–15, DOI 10.1046/j.1365-2486.1999.00009.x (1999).

65. M. J. Behrenfeld, P. G. Falkowski, Photosynthetic rates derived from satellite-based chlorophyll concentration. *Limnology and Oceanography* **42**, 1–20, DOI 10.4319/lo.1997.42.1.0001 (1997).

66. B. J. Mills, Y. Donnadieu, Y. Godderis, Spatial continuous integration of Phanerozoic global biogeochemistry and climate. *Gondwana Research* **100**, 73–86, DOI 10.1016/j.gr.2021.02.011 (2021).

67. A. J. West, Thickness of the chemical weathering zone and implications for erosional and climatic drivers of weathering and for carbon-cycle feedbacks. *Geology* **40**, 811–814, DOI 10.1130/G33041.1 (2012).

68. P. Maffre *et al.*, Mountain ranges, climate and weathering. Do orogens strengthen or weaken the silicate weathering carbon sink? *Earth and Planetary Science Letters* **493**, 174–185, DOI 10.1016/j.epsl.2018.04.034 (2018).

69. R. A. Berner, K. Caldeira, The need for mass balance and feedback in the geochemical carbon cycle. *Geology* **25**, 955–956, DOI 10.1130/0091-7613(1997)025<0955:TNFMBA>2.3.CO;2 (1997).

70. J. K. Caves, A. B. Jost, K. V. Lau, K. Maher, Cenozoic carbon cycle imbalances and a variable weathering feedback. *Earth and Planetary Science Letters* **450**, 152–163, DOI 10.1016/j. epsl.2016.06.035 (2016).

71. G. A. Shields, B. J. W. Mills, Tectonic controls on the long-term carbon isotope mass balance.
Proceedings of the National Academy of Sciences of the United States of America **114**, 4318–43232, DOI 10.1073/pnas.1614506114 (2017).

72. R. Berner, A model for atmospheric CO_2 over Phanerozoic time. *American Journal of Science* **291**, 339–376, DOI 10.2475/ajs.291.4.339 (1991).

73. L. R. Kump, M. A. Arthur, Interpreting carbon-isotope excursions: carbonates and organic matter. *Chemical Geology* **161**, 181–198, DOI 10.1016/S0009-2541(99)00086-8 (1999).

74. Y. Donnadieu *et al.*, A GEOCLIM simulation of climatic and biogeochemical consequences of Pangea breakup. Geochemistry, Geophysics, Geosystems **7**, Q11019, DOI 10.1029/2006GC001278 (2006).

75. K. Fraedrich, A suite of user-friendly global climate models: Hysteresis experiments. *The European Physical Journal Plus* **127**, 53, DOI 10.1140/epjp/i2012-12053-7 (2012).

76. O. Mehling, K. Bellomo, M. Angeloni, C. Pasquero, J. Von Hardenberg, High-latitude precipitation as a driver of multicentennial variability of the AMOC in a climate model of intermediate complexity. *Climate Dynamics* **61**, 1519–1534, DOI 10.1007/s00382-022-06640-3 (2023).

77. D. O. Gough, Solar interior structure and luminosity variations. *Solar Physics* **74**, 21–34 (1981).

78. E. Pucéat *et al.*, Revised phosphate–water fractionation equation reassessing paleotemperatures derived from biogenic apatite. *Earth and Planetary Science Letters* **298**, 135–142, DOI 10.1016/ j.epsl.2010.07.034 (2010).

79. S.-T. Kim, J. R. O'Neil, Equilibrium and nonequilibrium oxygen isotope effects in synthetic carbonates. *Geochimica et Cosmochimica Acta* **61**, 3461–3475, DOI 10.1016/S0016-7037(97)00169-5 (1997).

80. M. Daëron *et al.*, Most Earth-surface calcites precipitate out of isotopic equilibrium. *Nature Communications* **10**, 429, DOI 10.1038/s41467-019-08336-5 (2019).

81. L. Grossman, T.-L. Ku, Oxygen and carbon isotope fractionation in biogenic aragonite: temperature effects. *Chemical Geology* **59**, 59–74 (1986).

82. S. B. Malevich, L. Vetter, J. E. Tierney, Global core top calibration of ^{18}O in planktic foraminifera to sea surface temperature. *Paleoceanography and Paleoclimatology* **34**, 1292–1315, DOI 10.1029/2019PA003576 (2019).

83. J. E. Tierney, M. P. Tingley, A Bayesian, spatially-varying calibration model for the TEX_{86} proxy. *Geochimica et Cosmochimica Acta* **127**, 83–106, DOI 10.1016/j.gca.2013.11.026 (2014).

84. J. E. Tierney, S. B. Malevich, W. Gray, L. Vetter, K. Thirumalai, Bayesian calibration of the Mg/Ca paleothermometer in planktic foraminifera. *Paleoceanography and Paleoclimatology* **34**, 2005–2030, DOI 10.1029/2019PA003744 (2019).

85. M. Schobben *et al.*, Latest Permian carbonate carbon isotope variability traces heterogeneous organic carbon accumulation and authigenic carbonate formation. *Climate of the Past* **13**, 1635– 1659, DOI 10.5194/cp-13-1635-2017 (2017).

86. T. Westerhold *et al.*, Astronomical calibration of the Ypresian timescale: implications for seafloor spreading rates and the chaotic behavior of the solar system? *Climate of the Past* **13**, 1129–1152, DOI 10.5194/cp-13-1129-2017 (2017).

87. T. Westerhold, U. Rohl, B. Donner, J. C. Zachos, Global extent of early Eocene hyperthermal events: A new Pacific benthic foraminiferal isotope record from Shatsky Rise (ODP Site 1209). *Paleoceanography and Paleoclimatology* **33**, 626–642, DOI 10.1029/2017PA003306 (2018).